Turbulent channel flow of suspensions of neutrally buoyant particles over porous media

Parisa Mirbod[1]†, Seyed Mehdi Abtahi[1], Abbas Moradi Bilondi[1], Marco Edoardo Rosti[2], and Luca Brandt[3,4]

[1]Department of Mechanical and Industrial Engineering, University of Illinois at Chicago, 842 W. Taylor Street, Chicago, IL 60607, USA

[2]Complex Fluids and Flows Unit, Okinawa Institute of Science and Technology Graduate University, 1919-1 Tancha, Onna-son, Okinawa 904-0495, Japan

[3]Linne Flow Centre and SeRC, Department of Engineering Mechanics, KTH, Stockholm, Sweden

[4]Department of Energy and Process Engineering, Norwegian University of Science and Technology (NTNU), Trondheim, Norway

(Received xx; revised xx; accepted xx)

This study discusses turbulent suspension flows of non-Brownian, non-colloidal, neutrally buoyant, and rigid spherical particles in a Newtonian fluid over porous media with particles too large to penetrate and move through the porous layer. We consider suspension flows with the solid volume fraction Φ_b ranging from 0 to 0.2 and different wall permeabilities, while porosity is constant at 0.6. Direct numerical simulations (DNS) with an immersed boundary method (IBM) are employed to resolve the particles and flow phase, with the volume-averaged Navier-Stokes (VANS) equations modeling the flow within the porous layer. The results show that in the presence of particles in the free-flow region, the mean velocity and the concentration profiles are altered with increasing porous layer permeability because of the variations in the slip velocity and wall-normal fluctuations at the suspension-porous interface. Furthermore, we show that variations in the stress condition at the interface significantly affect the particle near-wall dynamics and migration toward the channel core, thereby inducing large modulations of the overall flow drag. At the highest volume fraction investigated here, $\Phi_b = 0.2$, the velocity fluctuations and the Reynolds shear stress are found to decrease, and the overall drag increases due to the increase in the particle-induced stresses.

Key words: Non-colloidal suspensions, Non-Brownian suspensions, Turbulent channel flow, Suspension flows over porous media

1. Introduction

The turbulent flow of suspensions over porous media is crucial in various environmental phenomena and industrial technologies. These include sedimentation in rivers, pyroclastic flows, flow through unconsolidated sand (Zhai *et al.* 2005), and hydraulic fracturing (Song *et al.* 2014). In these applications, both inertia and the presence of a porous surface play a critical role in the suspension dynamics and fluid-solid interactions. This study therefore

† Email address for correspondence: pmirbod@uic.edu

focuses on understanding how the permeability of a porous medium affects the dynamics of suspensions and the behavior of particles in a turbulent channel flow with a fixed porosity and porous layer thickness.

1.1. *Turbulent flows over porous media*

The flow over and through a porous medium with a complex structure can be examined by modeling the porous medium as a continuum with given physical properties (i.e., porosity and permeability). The porosity ε of a porous medium is defined as the ratio of its void volume to its bulk volume. Fractions and percentages can be used to express this dimensionless quantity. A porous material's permeability K, on the other hand, determines how well fluids can pass through it. A porous material with a high permeability allows fluids to flow more easily than one with low permeability. The permeability of a porous medium is related to the porosity, shape, and level of connections of the pores (Bear (1988)).

One of the first studies on flow through porous media was published by Darcy (1856). In his experiments, he demonstrated that the average flow rate flowing through sand (porous media) is proportional to the pressure gradient across it. Darcy's experimental data clearly demonstrated a linear relationship between average discharge rate and pressure gradient. The Darcy's law consists of two terms: one term can be interpreted as an average drag felt by the fluid as it passes through the porous medium and is balanced by the second term, which is the pressure gradient term. For the low porous Reynolds number for which Darcy's law hold, i.e., $Re_p << 1$, the flow is governed by Stokes' equation, in which the viscous term is responsible for the Darcy drag. A deviation from linearity is observed as Re increases. A nonlinear relationship was proposed by Forchheimer, with a quadratic drag term that better fits experimental data; the equation is called Forchheimer equation (Whitaker (1996*a*); Giorgi (1997); Joseph *et al.* (1982); Lage (1998)). As a result of inertial effects in the pores, the quadratic term appears in this equation. When the flow is no more governed by the Stokes equation, the quadratic drag term is due to the convective term, $(u \cdot \nabla)u$, in the Navier-Stokes equations.

Subsequently, Brinkman (1947) suggested to extend Darcy's law to high permeable materials by adding a sort of viscous term in the Stokes' equation. The Brinkman model has been studied over the years by different researchers interested in many different applications (see among others Neale & Nader 1974; Vafai & Thiyagaraja 1987; Vafai & Kim 1990; Hahn *et al.* 2002; Mirbod *et al.* 2009, 2017; Wu & Mirbod 2018, 2019; Haffner & Mirbod 2020; Kang & Mirbod 2021; Hooshyar *et al.* 2022). Importantly, Beavers & Joseph (1967) improved the Darcy equation to introduce interface jump conditions between liquid and porous media. In 1996, Whitaker derived the so-called Volume-Averaged Navier-Stokes (VANS) equations from the Navier-Stokes equations (NS) in a porous media (Whitaker 1996*b*). The VANS equations contain new terms, including the Darcy term, an average adhesion resistance, and the Forchheimer term, a second-order tensor due to the inertial effects of the resistance function of the geometric structure of the porous medium. It should be noted, however, that defining a model for the fluid-porous interface still remains a challenge. In fact, the structure of a porous medium modifies rapidly within the small layer next to the fluid-porous interface, i.e., the so-called Brinkman layer (Neale & Nader 1974); therefore, the Navier-Stokes averaging over a volume containing the interface is not consistent. To properly connect the VANS equations and the NS, Ochoa-Tapia & Whitaker (1995) introduced momentum-transfer conditions, which improved the computation of the transferred stress to both the fluid phase and the porous media. Here, in particular, we employ the Navier-Stokes equation for the free fluid flow and the Volume-Average Navier-Stokes equations inside the porous

media. These two equations are connected using the interface jump condition between liquid and porous media as proposed by Ochoa-Tapia & Whitaker (1995). It is worth noting that over the past 20 years, several groups have also tried to model the interface layer and control the momentum transfer (see e.g., Alazmi & Vafai 2001; Goyeau *et al.* 2003*a*; Chandesris & Jamet 2006; Valdés-Parada *et al.* 2007).

Both numerical and experimental works have been conducted to study the effect of isotropic and anisotropic porous materials on turbulent flows. Using a continuum approach for porous media, laminar and turbulent flows were investigated by Breugem *et al.* (2004). The authors showed that the permeability of the porous wall depends not only on the porosity but also on the gradient of the volume-averaged velocity inside the porous media. The same group later used DNS to investigate the turbulent channel flow over three-dimensional (3D) regular cubes mimicking porous structures (Breugem & Boersma 2005). They quantitatively showed that the VANS equations are able to accurately simulate the turbulent flows over and through permeable walls. They also analyzed the impact of a packed-bed porous wall on the turbulent channel flow (Breugem *et al.* 2006) and found the near-wall structures to be significantly different: streamwise-correlated streaks almost disappear while the spanwise vorticity near the wall increases for a highly permeable surface. This is consistent with the decrease in the peak value of the streamwise root-mean-squared (r.m.s.) velocity normalized by the friction velocity at the permeable wall. Furthermore, they showed that the turbulence near a highly permeable wall is dominated by relatively large vertical structures generated by a Kelvin-Helmholtz instability. Turbulent flows over porous media considering the porous layer as a continuum, without a need for knowledge of the porous media microstructure, have also been examined by Rosti *et al.* (2015, 2018). These authors also found that permeability plays a critical role and showed that porous materials with high wall-normal and low wall-parallel permeabilities are characterized by increased turbulence isotropy (Rosti *et al.* 2018). In a more recent work, Rosti *et al.* (2020) studied the flow inside a deformable porous medium for the case of a viscous fluid and an incompressible viscoelastic material. It was found that in a poroelastic medium the flow permeability is a function of the elastic shear modulus of the deformable surface and of the imposed pressure difference, suggesting that the dynamics of the flow over such a complex medium cannot be deduced directly from studies over rigid porous walls.

While most of the previous work discussed above considered isotropic porous media, anisotropic porous layers have been found to be effective for passive control of turbulence (see e.g. Gomez-de Segura *et al.* 2017; Rosti *et al.* 2018). Kuwata & Suga (2017) used multiple-relaxation-time (MRT) lattice Boltzmann DNS to simulate the turbulent flow over a porous layer. Considering anisotropic permeable walls and squared pore arrays aligned with the Cartesian axes, they found that streamwise and spanwise permeabilities considerably enhance the Reynolds stresses over the porous walls when compared to the vertical permeability. The turbulent channel flow over porous layers has also been studied experimentally (Suga *et al.* 2010, 2017); the authors showed that the spanwise scales of the measured structures can be reasonably correlated with the wall normal distance plus the zero-plane displacement, estimated from the mean velocity profile.

1.2. *Turbulent suspension flows over impermeable walls*

Particle-laden turbulent flows over impermeable walls have been extensively investigated. Many earlier studies considered small heavy particles in the very dilute regime. It has been shown that inertia induces particle preferential sampling and migrations that lead to clustering in both homogeneous and inhomogeneous flows (see among many Bec *et al.* 2007; Toschi & Bodenschatz 2009; Sardina *et al.* 2012).

Pan & Banerjee (1996) were the first to study the effect of finite-size particles in a turbulent channel flow at very low concentrations and showed that smaller particles decrease turbulence forces and Reynolds stresses, while larger particles increase turbulence intensities and stresses. These findings were in line with the other works that considered the effect of the particles on the spectral energy distribution and the turbulent cascade (Francesco Lucci & Elghobashi 2010; Yeo *et al.* 2010). The appearance of different numerical algorithms has facilitated an increasing number of studies on finite-size particles in turbulence. Among these, Kidanemariam *et al.* (2013) examined open channel flow with heavy particles of finite size in the dilute regime and showed that the solid phase is preferably assembled near the wall in low-speed regions. Later, the same approach was used by these authors to study pattern formation in turbulent channel flow over a mobile sediment bed (Kidanemariam & Uhlmann (2014)). Concerning neutrally buoyant particles in channel flow, Picano *et al.* (2015) studied neutrally buoyant spheres, while Ardekani & Brandt (2019) considered nonspherical particles, showing a reduced drag. The effect of particles on the critical Reynolds number for turbulence onset in semidilute suspension flows was studied in Matas *et al.* (2004); Loisel *et al.* (2013); Yu *et al.* (2013) and the chaotic flow of relatively dense suspensions of neutrally buoyant and heavy particles in channel flows, for a volume fraction of 7%, examined in Shao *et al.* (2012). Vowinckel *et al.* (2014) reported on various regimes that differ depending on the particle buoyancy. Recent studies conducted by us have examined both suspensions and solvent and their related instabilities over and through various porous media models in Bagheri *et al.* (2022); Haffner *et al.* (2019); Mirbod & Shapley (2022); Bagheri *et al.* (2019); Moradi Bilondi *et al.* (2022); Kang & Mirbod (2021). However, the impact of different porous media on non-Brownian, non-colloidal, neutrally buoyant, rigid, spherical particles flowing in a channel still remains unknown.

Thanks to recent developments in algorithms and computational power, suspension flows with inertia can be studied by interface-resolved direct numerical simulations (DNS), with ten thousand finite-size particles. Using fully resolved DNS and the Immersed Boundary Method (IBM) for neutrally buoyant spheres as conducted here, Lashgari *et al.* (2014) reported a transition akin to that found in the pure fluid case at low volume fractions, i.e., from the laminar base-state directly to turbulence as the Reynolds number was increased. However, a "shear-thickening" regime (distinct from laminar flow and turbulence) was identified when the volume fraction was sufficiently large, dominated by the particle induced stresses. Later, Picano *et al.* (2015) and Costa *et al.* (2016) observed that under fully turbulent conditions, significant particle-induced stress first appears at lower Φ_b in a layer close to the wall of size similar to the particle diameter; with increasing Φ_b, the wall-layer is characterized by large particle-induced stress and found to be responsible for the increased drag. These authors also reported that because of these nonhomogeneities in concentration distribution, the increase in the overall drag cannot be simply explained by using the notion of an increased effective suspension viscosity. The study by Ardekani *et al.* (2017) considered non-spherical oblate particles and showed that the drag is reduced, as these particles do not accumulate in the particle layer but remain away from the wall, confirming the importance of the particle dynamics in the near-wall region for the global flow behavior (see also Peng *et al.* 2019, for the role of particle rotation). Numerous direct numerical simulations have also been performed to examine the sediment transport of particle-laden flows over mobile and immobile beds (Jain *et al.* 2020, 2021; Vowinckel *et al.* 2014, 2017, 2021; Köllner *et al.* 2020; Vowinckel *et al.* 2019*a*,*b*; Biegert *et al.* 2017; Papadopoulos *et al.* 2020; Kempe *et al.* 2014; Herwig *et al.* 2011). Few studies, on the other hand, have investigated the particle flow over complex walls. Recently, Rosti *et al.* (2021) have investigated the rheology of

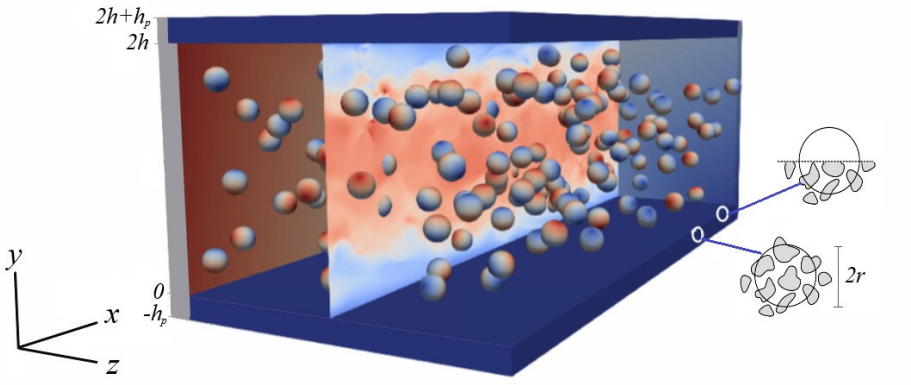

Figure 1. Sketch of the 3D channel flow with 50 particles overlying porous media followed by the coordinate system adopted in this study.

particle suspensions flowing over porous walls in a plane Couette flow and in a laminar regime; they found that the porous walls induce a progressive decrease in the suspension effective viscosity as the wall permeability increases. This behavior was explained by the weakening of the wall-blocking effect and by the appearance of a slip velocity at the interface of the porous medium.

1.3. *Outline*

This study employs DNS to simulate turbulent suspension flows of monodisperse, rigid, spherical particles over various porous media where particles interact with the porous layer but do not enter into it. The solid volume fraction considered varies in the range of $\Phi_b \in$ (0-0.2). We fully describe the solid phase dynamics via an IBM for the finite-size particles, with a ratio between the radius a and the channel half width h equal to 1/10 while solving the VANS equations for flow inside the porous media. The porous layer porosity and thickness are kept constant, while their permeability varies. The organization of the paper is as follows: Section 2 shows mathematical formulations, numerical procedures, system configuration, and related parameters. The results and discussions are presented in Section 3. Section 4 addresses the summary and conclusion of the study.

2. Methodology

2.1. *Governing equations*

We study the fully developed flow of mono-dispersed suspensions of rigid, spherical particles of radius a suspended in a Newtonian fluid in a channel bounded by identical, rigid, homogeneous, and isotropic porous media. The incompressible Navier-Stokes equations are used to describe the Eulerian fluid phase,

$$\nabla \cdot \mathbf{u}_f = 0 \tag{2.1}$$

$$\frac{\partial \mathbf{u}_f}{\partial t} + \mathbf{u}_f \cdot \nabla \mathbf{u}_f = -\frac{1}{\rho}\nabla p + \frac{\mu}{\rho}\nabla^2 \mathbf{u}_f + \mathbf{f}. \tag{2.2}$$

Here $\mathbf{u}_f$ and p represent the velocity and pressure fields, respectively, and the term $\mathbf{f}$ is a generic force field. In addition,the parameters μ and ρ are the dynamic viscosity and

the density of the fluid phase, respectively, and their ratio $\nu = \frac{\mu}{\rho}$ indicates the kinematic viscosity of the fluid. The centroid linear and angular velocities of neutrally buoyant particles, $\mathbf{u}_p$ and $\boldsymbol{\omega}_p$, are governed by the Newton-Euler Lagrangian equations, defined as

$$\rho_p V_p \frac{d\mathbf{u}_p}{dt} = \oint_{\partial V_p} (-p\mathbf{I} + \mu(\nabla \mathbf{u}_f + \nabla \mathbf{u}_f^T)) \cdot \mathbf{n} dA + \mathbf{F}_p \tag{2.3}$$

$$I_p \frac{d\boldsymbol{\omega}_p}{dt} = \oint_{\partial V_p} \mathbf{r} \times (-p\mathbf{I} + \mu(\nabla \mathbf{u}_f + \nabla \mathbf{u}_f^T)) \cdot \mathbf{n} dA + \mathbf{T}_p, \tag{2.4}$$

where ρ_p indicates the particle density and V_p is the particle volume, defined as $4\pi a^3/3$. In addition, $\mathbf{I}$ is the unit tensor, $I_p = \frac{2}{5}\rho_p V_p a^2$ is the moment of inertia, $\mathbf{r}$ is the distance vector from the center of the particle, and $\mathbf{n}$ is the unit vector normal to the particle surface ∂V_p. The terms $\mathbf{F}_p$ and $\mathbf{T}_p$ represent the force and torque acting on the particles as a result of the particle-particle and particle-wall interactions. To couple the solid and fluid phases, an IBM is used. This accounts for a body force $\mathbf{f}$ added to the right-hand side of (2.2) to mimic the actual no-slip and no-penetration boundary conditions at the moving particle surface (Breugem 2012; Picano *et al.* 2015; Ardekani *et al.* 2016),

$$\mathbf{u}_f|_{\partial V_p} = \mathbf{u}_p + \boldsymbol{\omega}_p \times \mathbf{r}. \tag{2.5}$$

We denote the porous layer with the porosity ε and the permeability with the tensor K_{ij}. When the porous medium is isotropic, the permeability reduces to a single scalar value, i.e., K. In this study, we employ the volume-average Navier-Stokes (VANS) equations to describe the fluid motion in the porous medium, as proposed by Whitaker (1969, 1986). For isotropic porous media with negligible fluid inertia and large-scale separation, the VANS equations can be stated as follows (Kang & Mirbod 2019; Rosti *et al.* 2021)

$$\nabla . \langle \mathbf{u}_f \rangle_s = 0 \tag{2.6}$$

$$\frac{\partial \langle \mathbf{u}_f \rangle_s}{\partial t} = -\frac{\varepsilon}{\rho} \nabla \langle p \rangle_f + \nu \nabla^2 \langle \mathbf{u}_f \rangle_s - \frac{\nu \varepsilon}{K} \langle \mathbf{u}_f \rangle_s, \tag{2.7}$$

Notably, the VANS equations are based on two different averaging methods (see Ochoa-Tapia & Whitaker 1995): the superficial volume average $\langle \psi \rangle_s = \frac{1}{V} \int_{V_f} \psi dV_f$ and the intrinsic volume average $\langle \psi \rangle_f = \frac{1}{V_f} \int_{V_f} \psi dV_f$ where the superficial and intrinsic volume average are linearly related to each other using the condition ε, $\langle \psi \rangle_s = \frac{V_f}{V} \langle \psi \rangle_f = \varepsilon \langle \psi \rangle_f$. Here V_f is the volume occupied by the fluid within the averaging volume V. Note that, superficial and intrinsic volume averages are employed for the velocity and pressure fields as reported by Quintard & Whitaker (1994) and Whitaker (1996*b*).

In our analysis, we assume pressure and velocity continuity at the suspension-porous interface, while the shear stress displays a jump that can be controlled by the parameter τ (Goyeau *et al.* 2003*a*; Ochoa-Tapia & Whitaker 1995; Rosti *et al.* 2021). The value of τ determines the stress transfer between the suspending fluid and the porous media. Consequently, the boundary conditions at the fluid-porous interface can be written as

$$\mathbf{u}_f = \langle \mathbf{u}_f \rangle_s \quad p = \langle p \rangle_f, \tag{2.8}$$

$$\sigma(\frac{\partial u_f}{\partial y} - \frac{1}{\varepsilon} \frac{\partial \langle u_f \rangle_s}{\partial y}) = \pm \tau u_f, \tag{2.9}$$

$$\sigma\left(\frac{\partial w_f}{\partial y} - \frac{1}{\varepsilon}\frac{\partial \langle w_f \rangle_s}{\partial y}\right) = \pm\tau w_f. \tag{2.10}$$

In eq. (2.8), $\mathbf{u}_f$ is the fluid flow velocity vector, while u_f and w_f in eq. (2.9) and eq. (2.10) are the streamwise and spanwise components of the fluid velocity, respectively. In eqs. (2.9) and (2.10), on the right-hand side, a positive sign indicates that the pure fluid region is above the porous media, while a negative sign indicates the opposite. The dimensionless parameter $\sigma = \frac{\sqrt{K}}{h}$ is the so-called Darcy number or the non-dimensional permeability parameter, where h is the half channel height. The coefficient τ represents the stress transfer between the suspending fluid and the porous media and takes varying values (zero, positive or negative), depending on how the porous material's structure varies in the heterogeneous transition layer and how the interface is fabricated. A detailed comparison of the different boundary conditions can be found in (Alazmi & Vafai (2001)). There were also several attempts to theoretically calculate τ (Goyeau *et al.* (2003*b*); Chandesris & Jamet (2006, 2007); Valdés-Parada *et al.* (2007, 2009); Deng & Martinez (2005); Min & Kim (2005); Carotenuto & Minale (2011)). Recently, also attempts to measure the jump coefficient were carried out by Carotenuto & Minale (2011) and by Bagheri & Mirbod (2022). In the present study, we assume τ=+1, 0 and -1. Note that τ= 0 implies that the stress carried by the suspending fluid is fully transferred to the fluid flow inside the porous layer. More details can be found in Sec. 3.3.

2.2. *Numerical implementation*

Our numerical simulations are based on a 3D solver that adopts an IBM for coupling the fluid and particle phases in the pure Newtonian fluid region, $0 < y < 2h$. The IBM method was first developed by Peskin (1972), who simulated blood flow patterns around the heart valves. Since then, it has been widely modified and improved, as reported in Mittal & Iaccarino (2005). Among others, Uhlmann (2005) proposed a direct forcing IBM and showed the ability of the method to simulate large-scale configurations with many particles. Here, we use the IBM as first proposed by Breugem (2012) while the various modifications introduced by this author enabled us to also reach second-order accuracy in space. It worth noting that, the IBM has a first-order accuracy in local velocity field and may have an apparent second-order accuracy in force/torque as reported by Peng & Wang (2020). Moreover, the particle-particle and particle-wall interaction force and torque in equations (2.3) and (2.4) include a lubrication correction and a soft collision model as reported in Costa *et al.* (2015). In particular, we use Brenner's asymptotic solution (Brenner (1961)) to correct the lubrication force when the distance between solid objects is less than a certain threshold and cannot be accurately resolved by the numerical mesh. At such small distances, surface roughness is accounted for by saturating this force. When spherical particles are in contact, both the normal and tangential contact force components are obtained from the overlap and the relative velocity. It worth noting that in this analysis, we considered the particles do not enter the porous layer. In other words, the particles approach an impermeable wall at the suspension-porous interface where the above lubrication and collision models can be applied.

The governing differential equations are solved on a staggered grid using a second-order central finite-difference scheme, while the dispersed phase is represented by a set of Lagrangian points that are uniformly distributed on the surface of each particle. The forces were computed at each Lagrangian grid point on the particle surface based on the difference between the computed velocity at the particle surface and the first prediction velocity of the fluid at the same point in space; the first prediction velocity was obtained by time integration of the free flow equations before imposing the continuity constraint.

ε	Re	σ	$\Phi_{\mathrm{b}}, (N_p)$	τ
0.6	5600	0.63×10^{-3}	0%	0
0.6	5600	2.00×10^{-3}	0%	0
0.6	5600	6.30×10^{-3}	0%	0
0.6	5600	0.63×10^{-3}	0%	+1
0.6	5600	0.63×10^{-3}	0%	−1
0.6	5600	0.63×10^{-3}	5%, (434)	0
0.6	5600	2.00×10^{-3}	5%, (434)	0
0.6	5600	6.30×10^{-3}	5%, (434)	0
0.6	5600	0.63×10^{-3}	10%, (868)	0
0.6	5600	2.00×10^{-3}	10%, (868)	0
0.6	5600	6.30×10^{-3}	10%, (868)	0
0.6	5600	0.63×10^{-3}	20%, (1736)	0
0.6	5600	2.00×10^{-3}	20%, (1736)	0
0.6	5600	6.30×10^{-3}	20%, (1736)	0
0.6	5600	0.63×10^{-3}	20%, (1736)	+1
0.6	5600	0.63×10^{-3}	20%, (1736)	−1

Table 1. List of simulations performed. The porosity is fixed at $\varepsilon = 0.6$ and the bulk Reynolds number is $Re = 5600$, whereas the non-dimensional permeability parameter and the solid volume fraction varies as indicated. The parameter N_p indicates the number of particles at each particle volume faction.

The forces are extrapolated on the Eulerian grid used for the momentum equations and added to the first prediction velocity, followed by the correction pressure scheme (Breugem 2012). For the time integration, we use the explicit fractional-step method, while all the other terms are advanced with the third-order Runge-Kutta scheme. More details in terms of the numerical procedures for both the IBM and VANS equations and the code validations can be found in Lashgari *et al.* (2014); Picano *et al.* (2015); Ardekani *et al.* (2016); Rosti & Brandt (2017); Izbassarov *et al.* (2018); Rosti *et al.* (2021).

2.3. *System Configuration*

Herein, we investigate turbulent suspensions flowing in a channel between two infinite walls located at $y = -h_p$ and $y = 2h + h_p$. The two porous layers have the thickness of h_p placed at the top and bottom of the channel, while the suspension-porous interface is located at $y = 0$ and $y = 2h$, see Fig. 1. Periodic boundary conditions are applied in the wall-parallel directions over a domain of size $L_x = 6h$, $L_y = 2(h + h_p)$, and $L_z = 3h$ in the streamwise, wall-normal, and spanwise directions, respectively. A time-dependent pressure gradient acting in the streamwise direction imposes a constant bulk velocity U_0 corresponding to a constant bulk Reynolds number, $Re = \frac{2hU_0}{\nu} = 5600$. For the simulations presented here, we use 960 grid points in the streamwise direction x, 320+32 grid points in the wall-normal direction y (where 32 is the number of points used for the porous layers), and 480 points in the spanwise direction z. The non-dimensional parameters and their values are as follows. The non-dimensional permeability parameter $\sigma \in [0.63, 6.3] \times 10^{-3}$, while the ratio between the porous and the channel height is $h_p/h = 1/10$ and the porosity of the porous layers is constant at 0.6. The ratio of particle diameter to channel height is $a/h = 1/10$ and the particle volume fraction ranges from 0

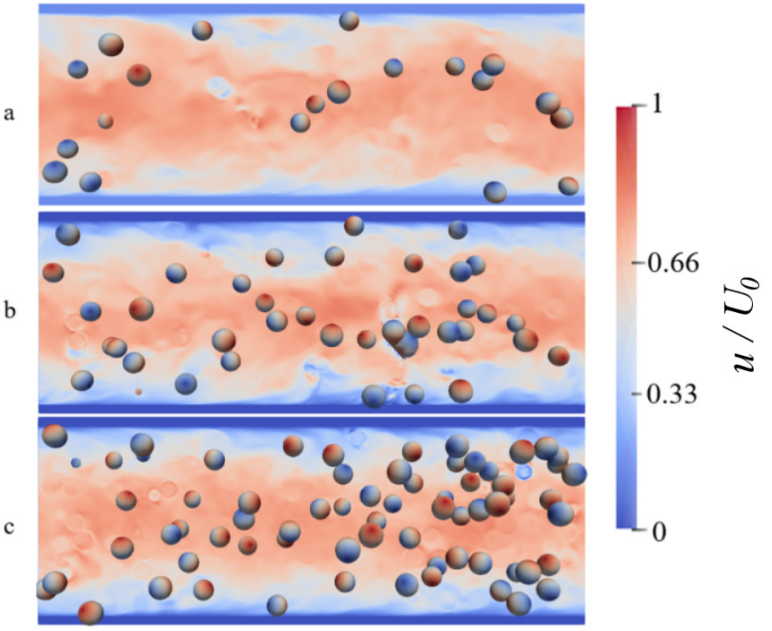

Figure 2. Contours of the instantaneous turbulent streamwise velocity u in the $x-y$ plane for a fixed wall non-dimensional permeability parameter, $\sigma = 0.63 \times 10^{-3}$ and three different particle volume fractions: (a) $\Phi_b = 0.05$, (b) $\Phi_b = 0.1$, and (c) $\Phi_b = 0.2$.

to 20%. Table 1 reports all different conditions considered in this study. For the sake of comparison, the simulation parameters are chosen similar to those in previous works on single-phase turbulent channel flows over porous walls and turbulent suspension flows in smooth channels as reported in Rosti *et al.* (2015); Picano *et al.* (2015); Rosti & Brandt (2017). All the simulations are started from a fully developed turbulent channel flow. After the flow has reached statistical steady state, the calculations are continued for an interval of $480h/U_0$ time units, during which 96 full flow fields are stored for further statistical analysis. To verify the convergence of the statistics, we have computed them using different number of samples and verified that the differences are negligible.

3. Results

We study the turbulent suspension flow of mono-dispersed, neutrally buoyant, rigid, spherical particles over porous media in a channel where the particles do not enter inside the porous layers. Figure 2 compares the contours of the normalized streamwise velocity component from instantaneous snapshots for the three different volume fractions under investigation. From the qualitative results shown in the figure, it can already be seen that the suspension flow streamwise velocity is sensitive to the particle volume fraction Φ_b. In particular, the turbulence activities are greatly enhanced throughout the channel due to the disturbances from the particles inside the channel. As the particle volume fraction increases, the streamwise velocity increases at the center of the channel; however, the velocity intensity decreases near the interface suggesting that the slip-velocity decreases when increasing the number of particles in the flow. Visualizations of the normalized streamwise velocity are shown in Figure 3 for three different wall non-

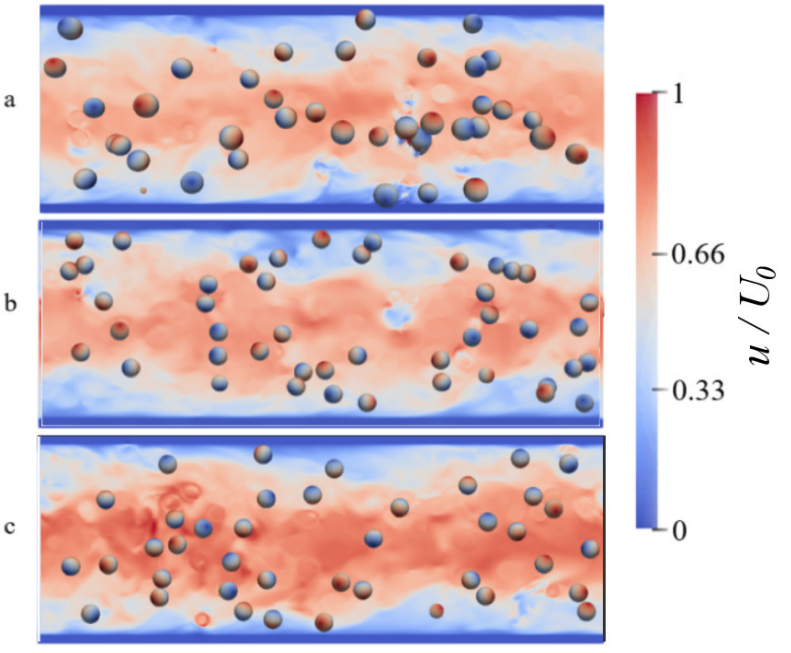

Figure 3. Contours of the instantaneous turbulent streamwise velocity u in the $x-y$ plane for a fixed particle volume fraction $\Phi_b = 0.10$ and three different wall non-dimensional permeability parameters: (a) $\sigma = 0.63 \times 10^{-3}$, (b) $\sigma = 2 \times 10^{-3}$, and (c) $\sigma = 6.3 \times 10^{-3}$.

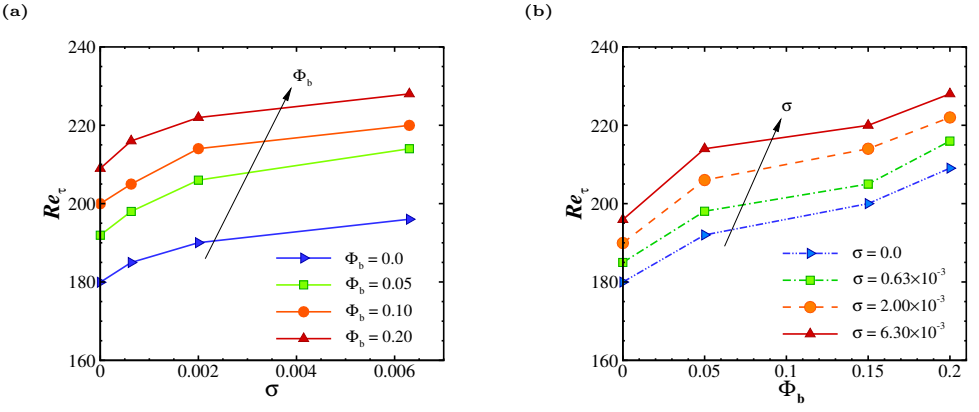

Figure 4. Friction Reynolds number Re_τ as a function of (a) wall non-dimensional permeability parameter σ, for different values of the particle volume fraction Φ_b, and as a function of (b) the particle volume fraction Φ_b for different values of wall non-dimensional permeability parameter σ.

dimensional permeability parameters σ. The wall permeability also has a critical impact on the turbulence suspension flows. By increasing the wall permeability, the turbulence activity is greatly enhanced throughout the channel. Clearly, as the wall permeability increases, the streamwise velocity intensity increases near the interface, which suggests that the slip-velocity increases by increasing the wall-normal velocity at the interface.

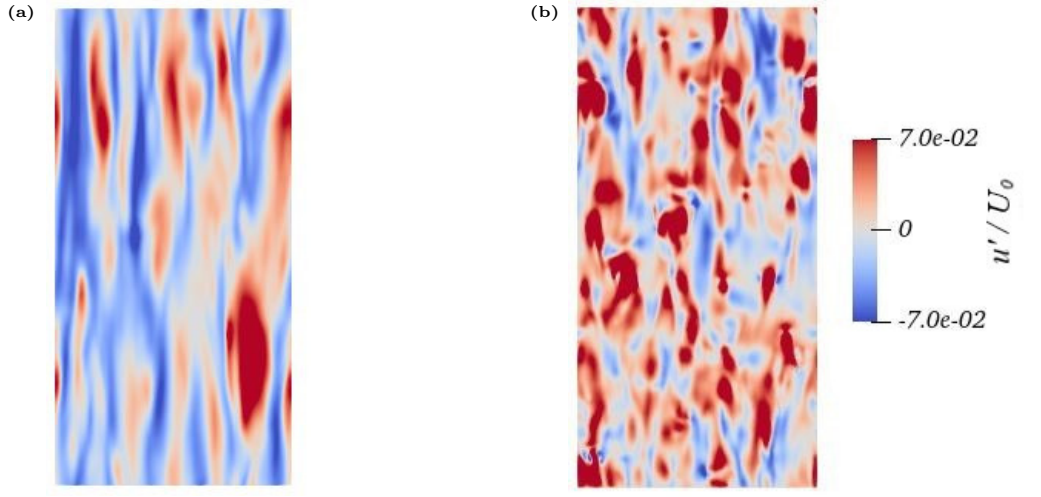

Figure 5. Instantaneous streamwise velocity fluctuation contours in the x-z plane at the interface $y = 0$ (flow going from bottom to top). (a) for solvent $\Phi_{\rm b}$=0.0 and (b) for suspension with the particle volume fraction $\Phi_{\rm b}$=0.1 at a fixed wall non-dimensional permeability parameter $\sigma = 0.63 \times 10^{-3}$.

3.1. *Flow statistics*

We start our quantitative analysis of the different suspension flows with the normalized pressure drop needed to drive the suspensions at a constant suspension flow rate. Figure 4 shows the friction Reynolds number Re_τ for all cases we considered in this study as a function of both the wall non-dimensional permeability parameter σ and the volume fraction $\Phi_{\rm b}$. The friction Reynolds number is based on the fluid viscosity that can be defined as $Re_\tau = u_\tau h/\nu$ where $u_\tau = \sqrt{\tau_{interface}/\rho}$ is the friction velocity and $\tau_{interface}$ is the total mean shear stress at the interface. The total mean shear stress at the interface is the sum of the viscous shear stress, the Reynolds shear stress, and the particle contribution (see Sec. 3.2 for more details). In the absence of particles, i.e., $\Phi_{\rm b} = 0$, the Re_τ increases with the wall permeability, as it was also observed in previous studies, e.g. (Rosti *et al.* 2015). Although some works (Hahn *et al.* 2002; Itoh *et al.* 2006) showed that a surface with preferential streamwise permeability might have a drag-reducing effect, permeable surfaces have generally been reported to increase the turbulent drag (Jimenez *et al.* 2001; Breugem *et al.* 2006; Rosti *et al.* 2015; Kuwata & Suga 2016). Our results are then consistent with previous works, observing a rise in turbulent drag compared to a smooth wall. Note that the skin friction coefficient of a pure fluid flow on porous walls was first studied by Ruff & Gelhar (1972) who experimentally showed that the skin friction coefficient is higher than that of impermeable walls. Later, several researchers (Kong & Schetz 1982; Zippe & Graf 1983) measured the increase in the skin friction coefficient over the porous layers and compared the results with the case of impermeable walls. These authors showed that the presence of a permeable wall reduces the turbulence intensity, Reynolds shear stress, pressure, and vorticity fluctuations throughout the channel except very near the wall. The results in Figure 4 also reveal that adding particles to the flow leads to a further increase in the friction Reynolds number Re_τ. It worth noting that the increase in drag has been associated with the appearance of Kelvin-Helmholtz-like rollers over the surface that increase both momentum transfer and the Reynolds stresses near the interface as shown in Figure 5 and reported in Jimenez *et al.* (2001); Breugem

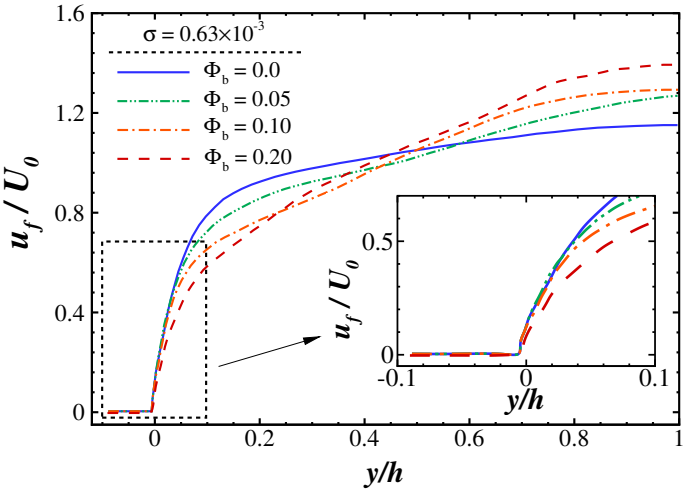

Figure 6. Mean fluid streamwise velocity component u_f normalized by the bulk velocity U_0 as a function of the wall-normal distance y for various particle volume fractions Φ_b at a fixed wall non-dimensional permeability parameter $\sigma = 0.63 \times 10^{-3}$.

et al. (2006); Rosti *et al.* (2015); Kuwata & Suga (2016). This figure shows snapshots of the fluctuating streamwise velocity at the free flow-porous interface for the cases of a pure solvent and flow with Φ_b=0.1 at a fixed $\sigma = 0.63 \times 10^{-3}$. The high and low velocity regions represent the footprints of the streaky pattern of the flow over the porous layer, shown in Figure 5a that are similar to those observed over smooth walls. A Kelvin-Helmholtz-like pattern is indicated by these streaky patterns, which are wider and have coherence structures when pure solvent is present. When particles are added to the flow, the coherent structures appear shredded over the porous layer, while the longitudinal streamwise vortices become more twisted. The Kelvin-Helmholtz-like rollers have been also analysed for the solvent flowing over both isotropic and anisotropic porous media in Rosti *et al.* (2018). These structures can be further detected and analysed from the two-point correlation functions as has been conducted by others (Jimenez *et al.* (2001); Kuwata & Suga (2016)), which is the subject of our future investigations.

Figure 6 shows the mean streamwise fluid velocity profiles for different particle volume fractions Φ_b and the non-dimensional permeability parameter $\sigma = 0.63 \times 10^{-3}$, the lowest considered in this study. Here, we observe that while the mean fluid velocity is blunted in the pure turbulent flow, it increases at the channel centerline when increasing the volume fraction, leading to a more laminar-like flow. In contrast, near the wall the fluid velocity decreases by increasing the particle volume fraction Φ_b; this effect is more pronounced for highly viscous suspension flows as shown in Rosti *et al.* (2021). Increasing the volume fraction does not modify the velocity inside the porous layer, i.e., for $y < 0$. This is because the wall permeability is very low and constant in this case and the particles are not moving inside the flow either; therefore, any disturbances produced by the particles rapidly vanish inside the porous layer. On the other hand, as expected and can be observed in figure 7 for a fixed particle volume fraction $\Phi_\mathrm{b} = 0.10$, by increasing the non-dimensional permeability parameter, the velocity inside the porous layer increases. In this case, for high wall permeability, the fluid moves easily inside the porous layer. Larger values of σ also result in higher slip velocity at the suspension-porous

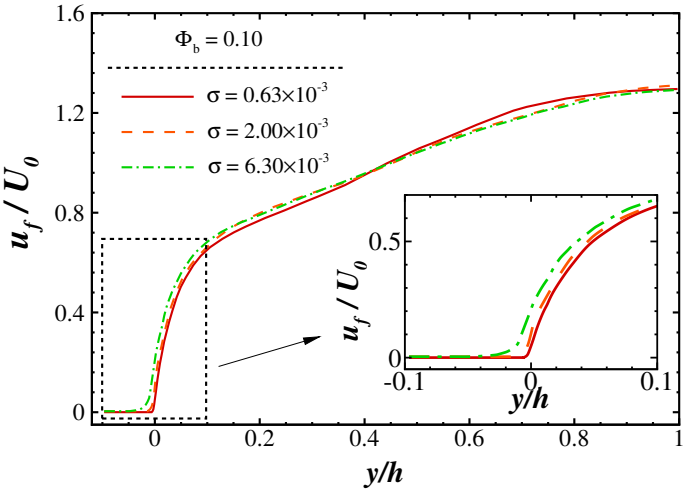

Figure 7. Mean fluid streamwise velocity component u_f normalized by the bulk velocity U_0 as a function of the wall-normal distance y for different values of the wall non-dimensional permeability parameter σ at a fixed particle volume fraction $\Phi_b = 0.10$.

interface (the velocity at $y = 0$). This increase in the slip velocity when increasing the wall non-dimensional permeability parameter from $\sigma = 0.63 \times 10^{-3}$ to $\sigma = 6.3 \times 10^{-3}$, see figure 7, implies that the local shear rate decreases with σ. Nevertheless, it appears that the parameter σ does not significantly affect the maximum velocity in the center of the channel and, in general, the velocity profile in the fluid region, $0 < y/h < 1$. Similar observations can be made by examining the data for the other volume fractions.

Both the presence of particles in the flow and the existence of the porous layers alter the velocity fluctuations in the bulk as well as at the wall. The root-mean-square (r.m.s) of the three fluid velocity fluctuations, normalized by the bulk velocity, are displayed in figure 8 for the wall non-dimensional permeability parameter $\sigma = 0.63 \times 10^{-3}$ and the different values of the particle volume fraction Φ_b. We note that a reduction in the fluid streamwise velocity fluctuations occurs with increasing volume fraction to $\Phi_b = 0.20$. On the other hand, the intensity of the cross-stream velocity fluctuations increases by adding particles in suspensions up to $\Phi_b = 0.1$, indicating that the presence of particles creates a more isotropic flow, and then decreases at the largest Φ_b considered, in agreement with the results for the flow over a rigid wall reported by Lashgari *et al.* (2014) and Picano *et al.* (2015) for smaller particles. Moreover, in the presence of particles, the Reynolds shear stress increases consistently up to $\Phi_b = 0.10$, as shown in panel (d) of the same figure. Upon further increasing the particle volume fraction to $\Phi_b = 0.20$, the Reynolds shear stress decreases, confirming a reduction in turbulent activity as shown in Picano *et al.* (2015) for the case of a solid wall. This reduction, however, is not associated with a decreased drag because the larger particle stresses at higher Φ_b more than compensate for the lower turbulence levels. The results pertaining to the flow over a porous wall confirm this picture, with some differences, as will be further discussed below.

The variation of the root-mean-square (r.m.s) of the fluid velocity fluctuations with the wall non-dimensional permeability parameter σ is depicted in Figure 9 for the flows at particle volume fraction $\Phi_b = 0.10$. The magnitude of the root-mean-square (r.m.s) of all the fluid velocity fluctuations increases with the wall permeability, consistent with

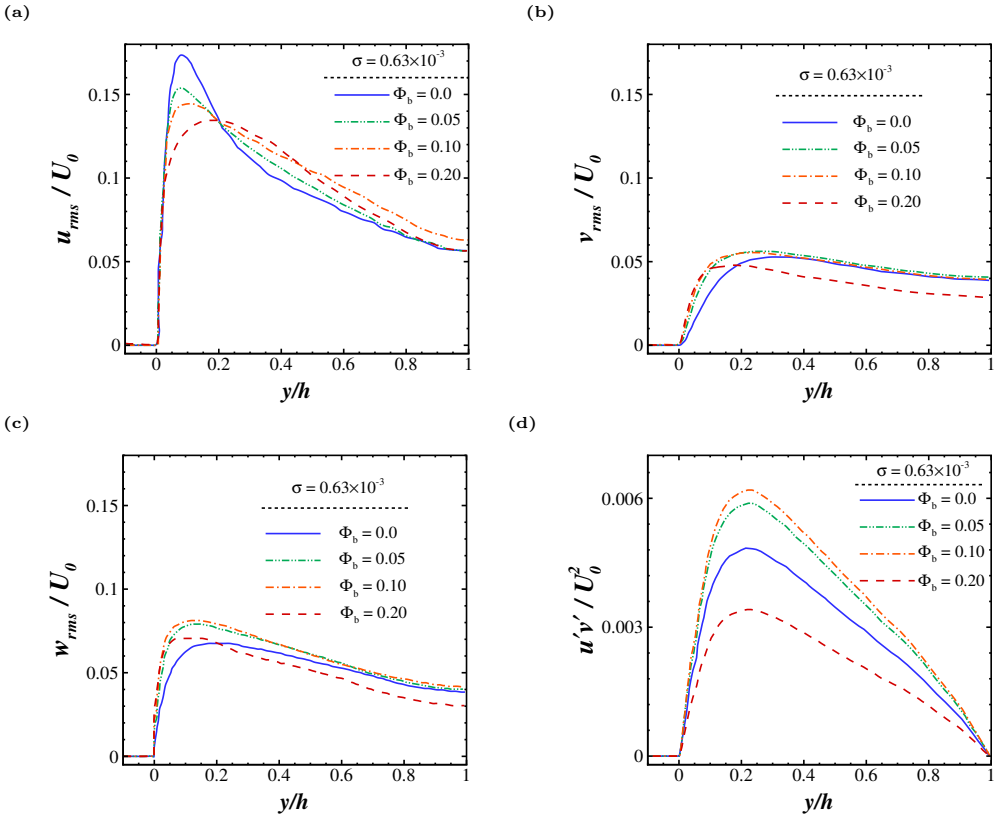

Figure 8. Intensity of the fluid fluctuation velocity components normalized by U_0 and the Reynolds shear stress for different particle volume fractions and non-dimensional permeability parameter $\sigma = 0.63 \times 10^{-3}$: (a) Streamwise u_{rms}, (b) wall-normal v_{rms}, and (c) spanwise w_{rms} velocity fluctuations; and (d) shear stress $(uv)'$.

previous studies for single-phase flows (Breugem *et al.* 2006; Rosti *et al.* 2015) where the increase in the streamwise velocity component is larger than that of the wall-normal and spanwise velocity fluctuations. In the boundary layer above the permeable wall, a sharp increase in the r.m.s velocities is observed when compared to the layer below the permeable wall, as also seen for the spanwise and wall-normal wall fluctuations. This can be attributed to the strengthening of the viscous effects near a permeable wall (Perot & Moin 1995). Note that due to the fact that the r.m.s. values of true local velocities inside the permeable walls are negligible, we can therefore assume that the turbulent flow in the channel is not significantly affected either by the thickness of the porous layer or by the distance to the solid wall.

The results suggest that the particle dynamics are indeed modified by the wall permeability and, in turn, the particle motion modifies the flow. Figure 9 (d) shows the profiles of the Reynolds stresses for different values of the wall non-dimensional permeability parameter σ, normalized by the bulk velocity, U_0^2. The maximum shear stress occurs near the interface with the permeable wall. The data also show that the Reynolds shear stress increases with the wall permeability. This confirms that, for the higher wall permeability, the weakening of the wall-blocking effect causes a strong increase in the Reynolds shear stress as reported by Breugem *et al.* (2006). In other words, fluid with high streamwise

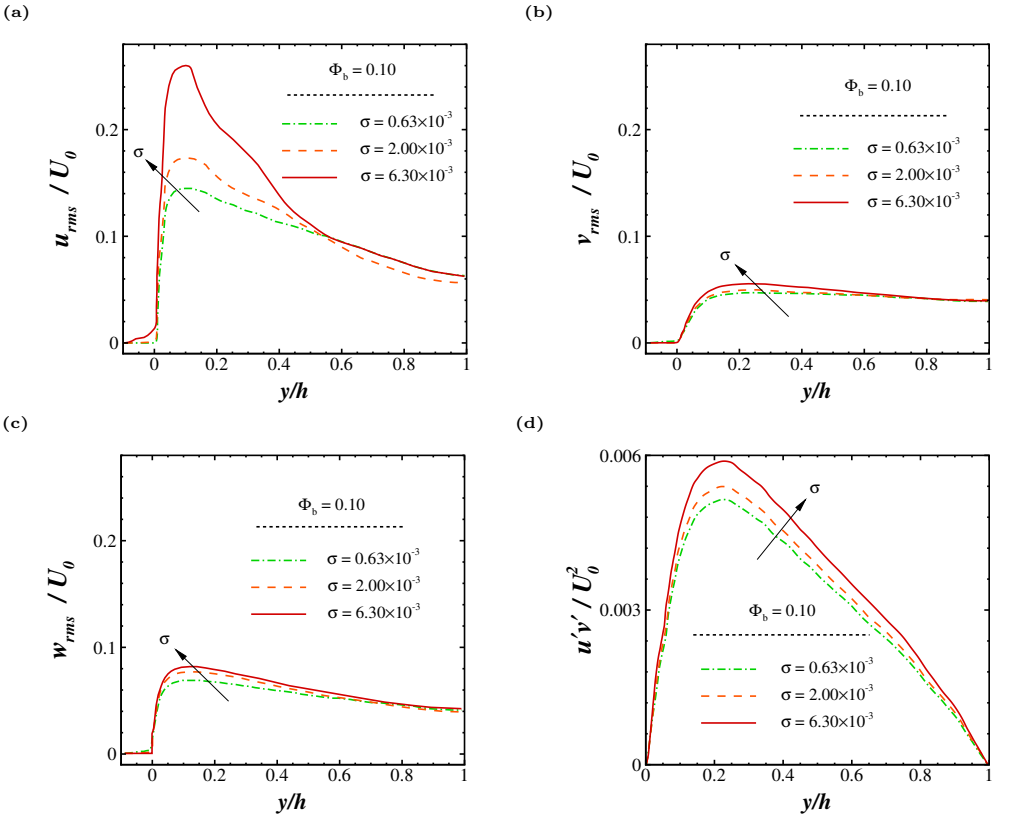

Figure 9. Intensity of the fluid fluctuation velocity components normalized by U_0 and the Reynolds shear stress for $\Phi_b = 0.10$ and different values of the wall non-dimensional permeability parameter: (a) streamwise u_{rms}, (b) wall-normal v_{rms}, (c) spanwise w_{rms} velocity fluctuations, and (d) shear stress $(uv)'$.

momentum may penetrate inside the porous surface, while to satisfy the conservation of mass, the fluid with relatively low streamwise momentum is transported from the porous region into the channel.

The slip velocity u_s at the interface, $y = 0$, normalized by the bulk fluid velocity is shown in Figure 10(a) for different values of the wall non-dimensional permeability parameter and of the particle volume fraction. As expected, by increasing the non-dimensional permeability parameter σ, the slip velocity increases, while with increasing particle volume fraction it decreases for all cases studied here. Interestingly, for $\Phi_b \leqslant 0.10$, the slip velocity is weakly dependent on the volume fraction, and it is mainly determined by the permeability under dilute conditions. Indeed, a more significant variation in the u_s values is observed when further increasing the dispersed phase concentration to 0.2. These results confirm that the suspension slip velocity in turbulent flows depends on the porous permeability, and when the porous non-dimensional permeability parameter is low, i.e., on the order of σ=$\mathcal{O}(10^{-4})$, the slip velocity depends mainly on the suspension concentration.

We then characterized the normalized wall-normal velocity fluctuations at the interface for different values of the wall non-dimensional permeability parameter σ and the particle volume fraction Φ_b as shown in Figure 10(b). The wall-normal velocity fluctuations

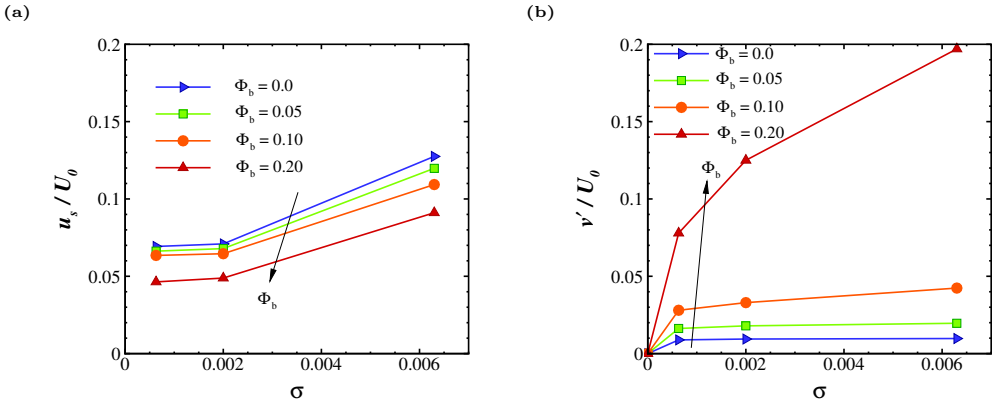

Figure 10. (a) Normalized interface slip velocity as a function of the wall non-dimensional permeability parameter σ for the different particle volume fractions under investigation and (b) normalized interface wall-normal fluctuation velocity as a function of the wall non-dimensional permeability parameter σ for different particle volume fractions.

increase with both the particle volume fraction and the wall permeability, from zero for small wall permeability to the largest value for the highest Φ_b. Note that the velocity fluctuations at the suspension-porous interface do not change significantly with the values of σ investigated; instead, the effect of the particle volume fraction is more pronounced with a more significant increase for $\Phi_b = 0.2$. Comparing the two panels in Figure 10, one can conclude that the mean slip at the wall is mainly determined by the wall permeability, while the velocity fluctuations are significantly influenced by the particle dynamics in the free-flow region.

To further understand how turbulent structures are modified by the presence of both porous media and particles, we examine some basic features of turbulent coherent structures. As shown in Rosti & Brandt (2020), the turbulent fluctuations are generally reduced and the flow is very anisotropic in the case of drag reduction. On the other hand, the presence of particles causes the opposite effect, i.e., more isotropic structures. Here, in particular, we study the effect of wall permeability on the distribution of the wall-normal and streamwise fluctuation velocity. Figure 11 shows the joint probability distribution functions (PDFs) of the wall-normal and streamwise fluctuation velocity at the interface of the porous layer and suspensions between the center of the channel and the interface and also at the centerline of the channel for the flows at particle volume fraction $\Phi_b = 0.10$ and the three wall non-dimensional permeability parameters under consideration. The ejection and sweep events are disrupted by increasing the wall permeability, leading to a decrease in the streamwise velocity fluctuations u' and an increase of the wall-normal component v'. These results show that permeability creates a more isotropic flow; this has been associated with drag increase as reported in several previous studies, e.g., Breugem *et al.* (2006). Note also that the differences are minor in the channel centreline. Similarly, figure 12 shows the joint probability distribution functions (PDFs) of the wall-normal and streamwise fluctuation velocity at the suspension flow-porous interface, between the center of the channel and the interface, and at the centerline of the channel for the flows at wall non-dimensional permeability parameter $\sigma = 0.63 \times 10^{-3}$ for different particle volume fractions. As observed, the presence of particles induces a disruption of the structures in the near wall region, resulting in a decrease in u' and an increase in v', leading to an overall more isotropic state. In other words, both wall permeability and the presence of dispersed

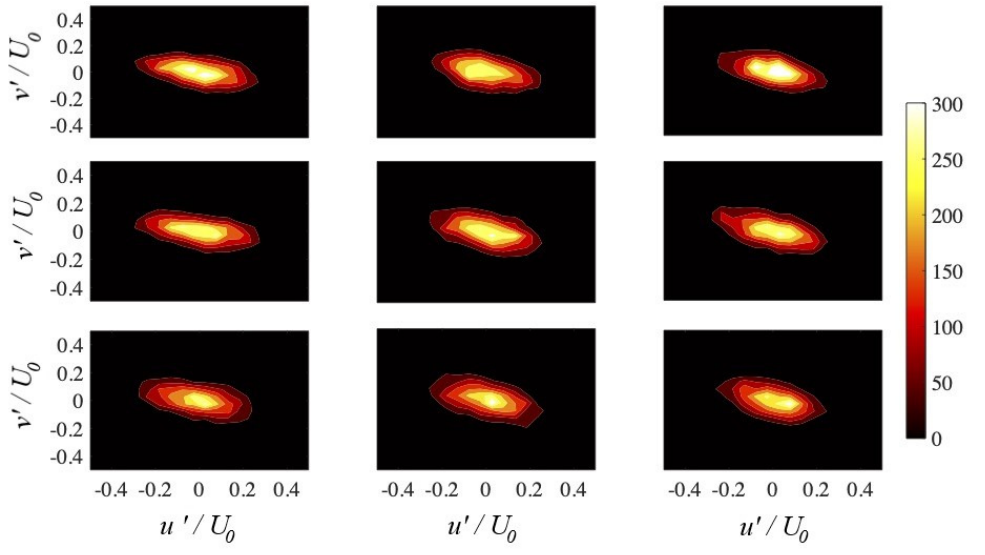

Figure 11. Normalized probability distribution function (PDF) of the streamwise fluctuation velocity u' and wall-normal fluctuation velocity v' for a fixed particle volume fraction $\Phi_b = 0.10$ and various non-dimensional permeability parameters. (top) $\sigma = 0.63 \times 10^{-3}$, (middle) $\sigma = 2.0 \times 10^{-3}$, and (bottom) $\sigma = 6.3 \times 10^{-3}$. From left to right: at the flow-porous interface, between the center of the channel and the interface, and at the centerline of the channel.

particles induce a more isotropic flow. However, as discussed above, the increase in wall permeability also leads to an increase in the turbulent Reynolds stresses, while the more isotropic turbulence due to the presence of the particles is associated with less correlated motions, i.e. lower Reynolds stresses (cf. panel d of figs. 8 and 9).

3.2. *Particle dynamics and stress budget*

In this section, we investigate the particle dynamics in turbulent channel flow in the presence of porous walls. In the case of spherical particles, the formation of a particle wall layer and the rotation rate close to the wall are shown to have a significant impact on the turbulent global drag (Costa *et al.* 2016, 2018; Peng *et al.* 2019). Indeed, in the presence of an elastic wall, particles are shown to migrate away from the wall, which significantly reduces the overall pressure drop (Ardekani *et al.* 2019). Figure 13(a) shows the mean local volume fraction ϕ for the case of wall non-dimensional permeability parameter $\sigma = 0.63 \times 10^{-3}$ and the three nominal volume fractions Φ_b investigated, while panels (b,c) display how the particle distribution changes with the permeability for two different values of the particle volume fraction. Note that the oscillations in Figure 13(b,c) can be attributed to particle layering close to the interface and, as the particle diameter is 0.2, these oscillations occur one, two, or three times the particle diameter.

Overall, we note the formation of a first local maximum close to the interface, associated with the particle-wall layers in the free-flow region. As also observed in highly dense suspensions in laminar flows (Yeo & Maxey 2010), the intensity of the particle wall layer increases as the particle volume fraction increases (see panel (a) of the figure). Its formation is explained by the solid lubrication interactions when a particle reaches the wall, which stabilizes the near-wall particle position; once close to the wall, the motion of

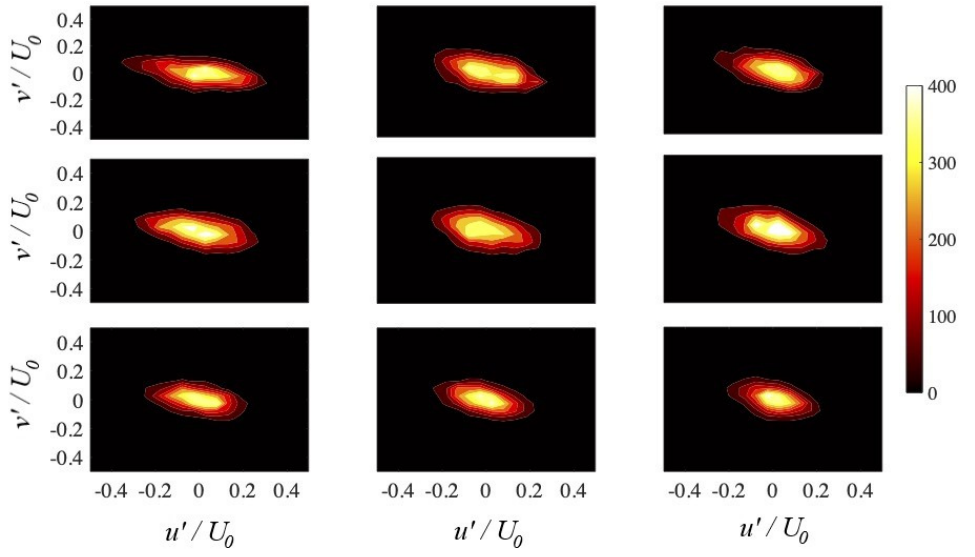

Figure 12. Normalized probability distribution function (PDF) of the streamwise fluctuation velocity u' and wall-normal fluctuation velocity v' at the interface for a fixed wall non-dimensional permeability parameter $\sigma = 0.63 \times 10^{-3}$ and various particle volume fractions, (top) particle volume fraction $\Phi_b = 0.05$, (middle) $\Phi_b = 0.10$, and (bottom) $\Phi_b = 0.20$. From left to right: at the flow-porous interface, between the center of the channel and the interface, and at the centerline of the channel.

finite-size particles is mainly influenced by collisions with other particles. Consequently, it is difficult for particles belonging to the first layer to escape.

In the presence of a permeable wall, we note weak migrations of particles away from the wall and a less pronounced wall layer for $\Phi_b = 0.05$ and 0.10, with the peak value close to the wall found to decrease with the permeability, consistent with the observation of increased wall-normal fluctuations (see also Ardekani *et al.* 2019, for the case of suspension flows over elastic walls). Note that these near-wall maxima are on the order of the bulk concentrations and are not related to the turbophoretic drift observed in dilute suspensions of heavy particles (Reeks 1983). The same trend observed here was reported in Rosti *et al.* (2021) for laminar Couette flow of suspensions over a porous substrate. Finally, we also see an increase in the local volume fraction ϕ toward the channel centreline for the largest volume fraction examined, $\Phi_b = 0.20$. This migration toward the channel core was observed experimentally in turbulent flows over solid walls and related to inertial effects in Zade *et al.* (2018). The accumulation toward the centreline was also associated with quenching of the turbulence fluctuations and reduced mixing (Ardekani *et al.* 2018; Yousefi *et al.* 2021).

To further examine the global suspension behavior, we look at the streamwise momentum budget. The total momentum budget in the free-flow region (i.e., $0 < y < 2h$) can be written as the sum of the viscous stress, the Reynolds stress, and the particle contribution (see Picano *et al.* 2015, for more details and derivations) as

$$\tau = \tau^{visc} + \tau^{reyn} + \tau^{part}. \tag{3.1}$$

Here, τ is the mean total shear stress balancing the imposed pressure gradient, $\tau^{visc} =$

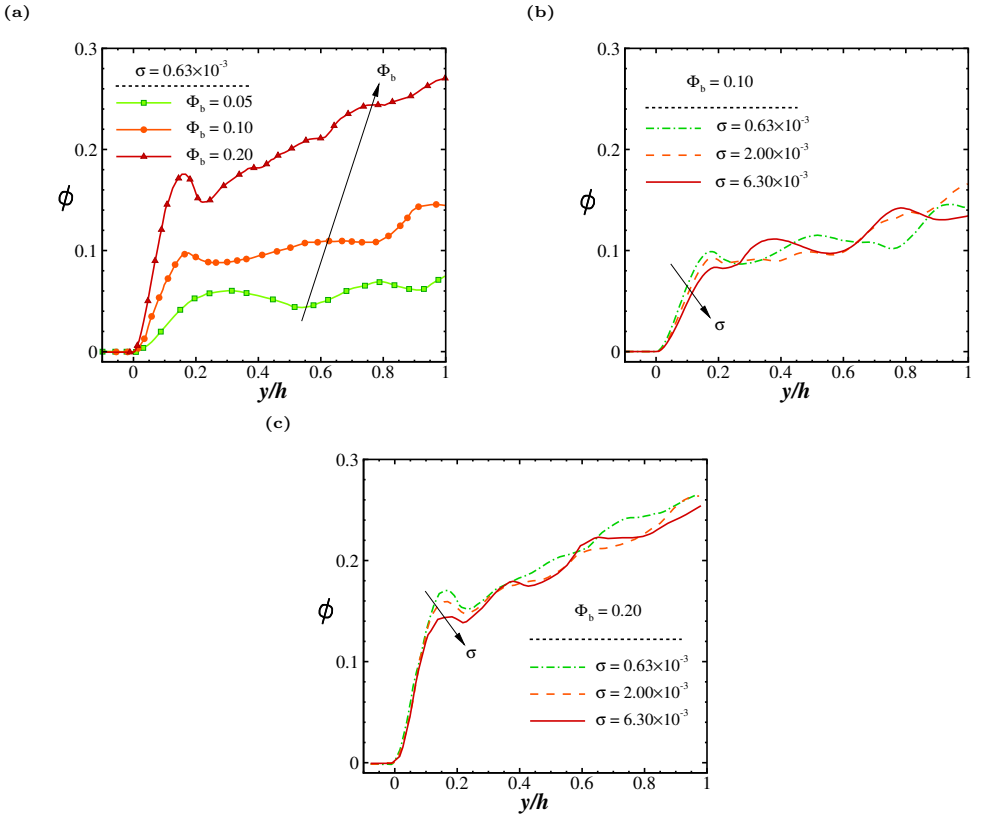

Figure 13. Average particle concentration ϕ as a function of the wall-normal distance y for (a) different particle volume fractions at fixed non-dimensional permeability parameter $\sigma = 0.63 \times 10^{-3}$; (b) and (c) various wall non-dimensional permeability parameters σ at fixed particle volume fractions $\Phi_\mathrm{b} = 0.10$ and 0.20.

$\mu \frac{du}{dy}$ is the viscous shear stress, $\tau^{reyn} = -\rho(uv)'$ is the Reynolds shear stress associated to the fluid and particle velocity correlation. τ^{part} is the particle contribution, including particle collisions, which was found by subtracting the other two components from the total shear stress.

The different contributions to the total shear stress in the turbulent suspension flows are displayed for the different particle volume fractions and wall non-dimensional permeability parameter $\sigma = 0.63 \times 10^{-3}$ in figure 14(a) and for $\sigma = 6.3 \times 10^{-3}$ in figure 14(b). Overall, we note that the relative viscous stress varies weakly with both the volume fraction and the wall permeability, whereas the percentage contribution of turbulence decreases with Φ_b. Although the level of fluctuations increases up to $\Phi_\mathrm{b} = 0.1$, the turbulent stress decreases because these chaotic motions are less correlated. The contribution associated with the particle stresses increases with Φ_b, differently for different permeabilities. In particular, we see a significant increase when increasing from 0.05 to 0.1 at the lowest permeability, and the most significant growth at $\Phi_\mathrm{b} = 0.2$ at the highest permeability studied. This suggests that the weakening of the particle wall layer is responsible for the reduced turbulent transport at low values of Φ_b, which is more significant at lower values of the wall permeability. On the other hand, the particle accumulation toward the channel core by inertial collisions is responsible for the

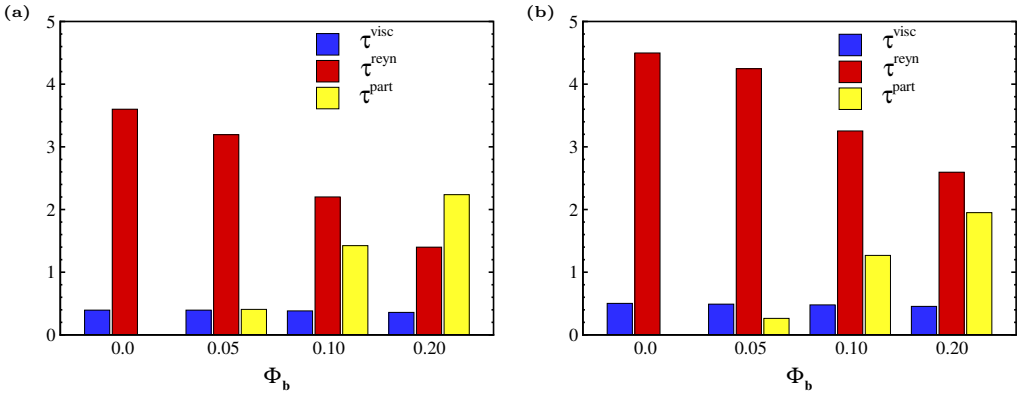

Figure 14. Histograms showing the different components of the mean shear stress balance as a function of the particle volume fraction Φ_b for (a) $\sigma = 0.63 \times 10^{-3}$ and (b) $\sigma = 6.3 \times 10^{-3}$. Blue, red and yellow show the viscous stress, Reynolds shear stress, and particle contributions, respectively.

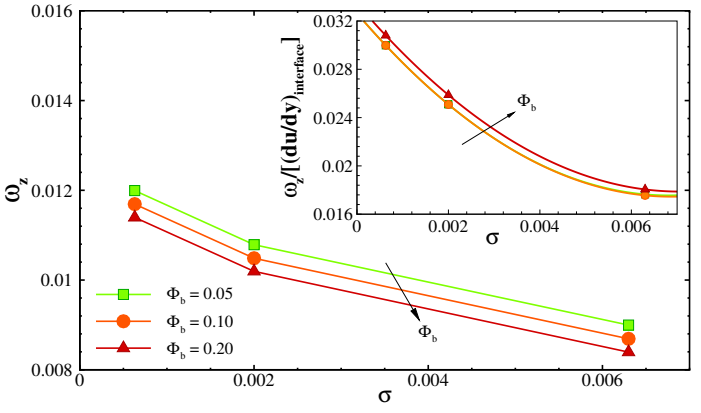

Figure 15. Spanwise component of the near-wall particle angular velocity as a function of the wall non-dimensional permeability parameter σ for different volume fractions $\Phi_b = 0.05$, $\Phi_b = 0.10$, and $\Phi_b = 0.20$.

reduction of the turbulence activity at $\Phi_b = 0.2$, an effect more weakly dependent on the wall permeability, cf. panel (a) and (b) of figure 14. To summarize, the main contribution to the total shear stress is the particle stress at high concentrations, while the Reynolds stress contribution is higher for lower concentrations. The viscous shear stress remains constant for all the volume fractions and the different wall permeabilities considered here. The values of viscous stress are small compared to the two other components because of the turbulent flow considered here, despite the moderate Reynolds number. Focusing on the effect of permeability, the particle-stress contribution decreases with increasing wall non-dimensional permeability parameter σ, whereas the Reynolds stress shows the opposite behavior, i.e., it decreases with the volume fraction Φ_b and increases with the wall non-dimensional permeability parameter σ because of the increase in fluctuations at the interface.

Figure 15 displays the spanwise component of the mean particle angular velocity for different particle volume fractions as a function of the wall permeability, where the values are averages over all the particles close to the interface, i.e., $y/h = 0.05$. It can be

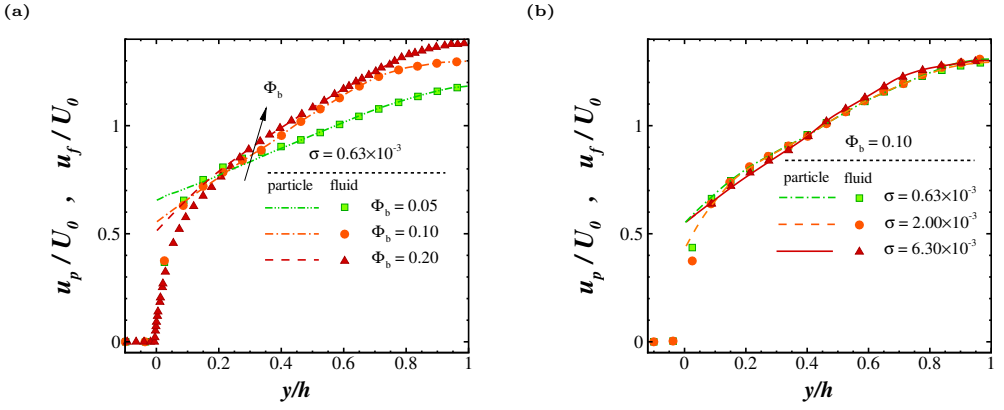

Figure 16. Mean particle streamwise velocity component u_p normalized by the bulk velocity U_0 as a function of the wall-normal coordinate y (lines), (a) for various particle volume fractions Φ_b at a fixed wall non-dimensional permeability parameter $\sigma = 0.63 \times 10^{-3}$, and (b) for various wall non-dimensional permeability parameters σ at a fixed particle volume fraction $\Phi_\mathrm{b} = 0.10$. The symbols represent the mean fluid velocity profiles.

revealed that the particle averaged angular velocity decreases by increasing the wall non-dimensional permeability parameter σ. As expected, this is because the near-wall shear decreases with permeability as discussed above. In addition, we note that the spanwise component of the mean particle angular velocity decreases with the particle volume fraction Φ_b as observed in previous studies (Ardekani & Brandt 2019). However, this effect is small in comparison with the variations induced by the wall permeability. In brief, with increasing wall permeability, the particle rotation decays; consequently, this causes a reduction in particle-induced interactions. The inset of Figure 15 plots the ratio of particle angular velocity with respect to the fluid shear rate as a function of bulk particle volume fraction Φ_b for various permeability parameter σ. Interestingly, the data in the main panel of Figure 15 for both $\Phi_\mathrm{b} = 0.05$ and $\Phi_\mathrm{b} = 0.1$ are now collapsed onto a curve $\omega_z/[(du/dy)_{interface}] = 0.03346 - 4.419\sigma + 313.3\sigma^2$ that has been determined from a polynomial fit data. There is, however, a higher ratio for Φ_b=0.2. At Φ_b=0.2, the fluid shear rate is lower, as shown in Figure 6, and the induced particle velocity and angular velocity are both affected by particles gathered at the interface.

Figure 16(a) shows the mean streamwise particle velocity profiles for different volume fractions Φ_b at a fixed wall non-dimensional permeability parameter $\sigma = 0.63 \times 10^{-3}$, while Figure 16(b) displays the particle velocity profile for different wall non-dimensional permeability parameters and a fixed particle volume fraction, $\Phi_\mathrm{b} = 0.10$. Comparing the mean particle velocity profiles (lines) with the mean fluid velocity values (symbols) indicates that the mean particle velocity and mean fluid velocity profiles are comparable inside the free-flow region except near the porous wall where the mean particle velocity is larger than the mean local fluid velocity. Although the fluid velocity at the interface is almost zero, the particle velocity differs due to the lack of the no-slip condition, resulting in a greater particle velocity than the fluid velocity.

3.3. *Effect of the momentum transfer coefficient* τ

We now investigate the modification induced on the turbulence statistics by varying the coefficient τ, which is used for the momentum-transfer conditions at the flow-porous interface. This coefficient can be related to the unknown structure of the suspending fluid-porous interface. As mentioned above, the value of τ determines the stress transfer

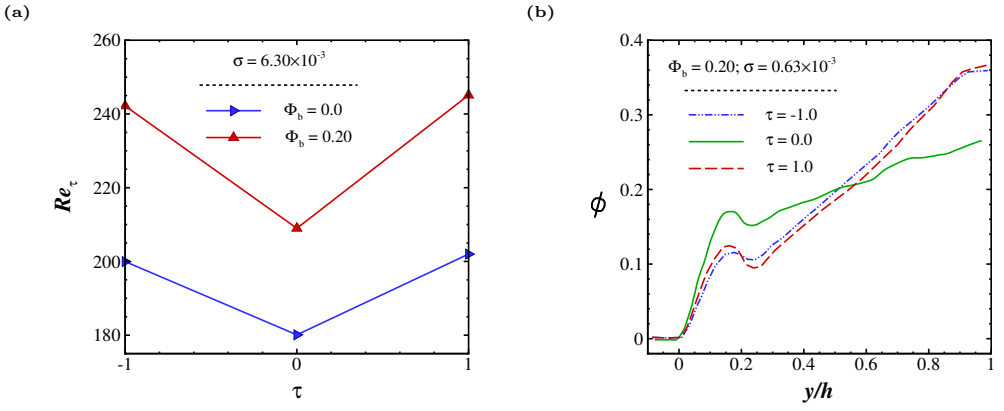

Figure 17. (a) Friction Reynolds number Re_τ as a function of τ, for different particle volume fractions $\Phi_\mathrm{b} = 0$ and 0.2. (b) Average particle concentration ϕ as a function of the wall-normal distance y for different τ at a fixed non-dimensional permeability parameter $\sigma = 0.63 \times 10^{-3}$.

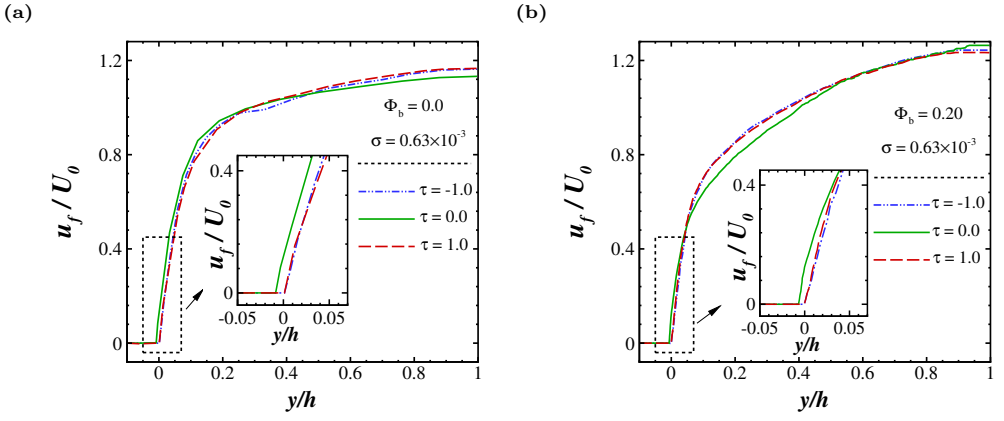

Figure 18. Mean fluid streamwise velocity component u_f normalized by the bulk velocity U_0 as a function of the wall-normal distance y for different values of momentum transfer coefficient τ and wall non-dimensional permeability parameter $\sigma = 0.63 \times 10^{-3}$. (a) Pure fluid ($\Phi_\mathrm{b} = 0$), (b) $\Phi_\mathrm{b} = 0.20$.

between the suspending fluid and the porous media. This was first introduced by Ochoa-Tapia & Whitaker (1995) as an additional boundary condition at the interface; it is order one and can be both positive or negative. It was further characterized by Ochoa-Tapia & Whitaker (1995); Valdés-Parada *et al.* (2007, 2013); Minale (2014*a*,*b*); Chen *et al.* (2016). In particular, Minale (2014*a*,*b*) showed that a negative τ quantifies the amount of stress transferred from the free fluid to the porous matrix, while a positive τ quantifies the amount of stress transferred from the porous matrix to the free fluid, whereas $\tau = 0$ represents the case in which the stress carried by the free fluid is fully transferred to the fluid saturating the porous matrix. Here, we consider the flow of a pure fluid, $\Phi_\mathrm{b} = 0$, and a dense suspension, $\Phi_\mathrm{b} = 0.20$, for comparison; we expect that the turbulence statistics for other volume fractions fall within these two cases. The porous layer non-dimensional permeability parameter is fixed at $\sigma = 0.63 \times 10^{-3}$ and the porosity is $\varepsilon = 0.6$, again with Reynolds number $Re = 5600$. We compare data from three values of τ, i.e., $-1, 0$, and 1, chosen because the momentum transfer coefficient τ falls in this range for most

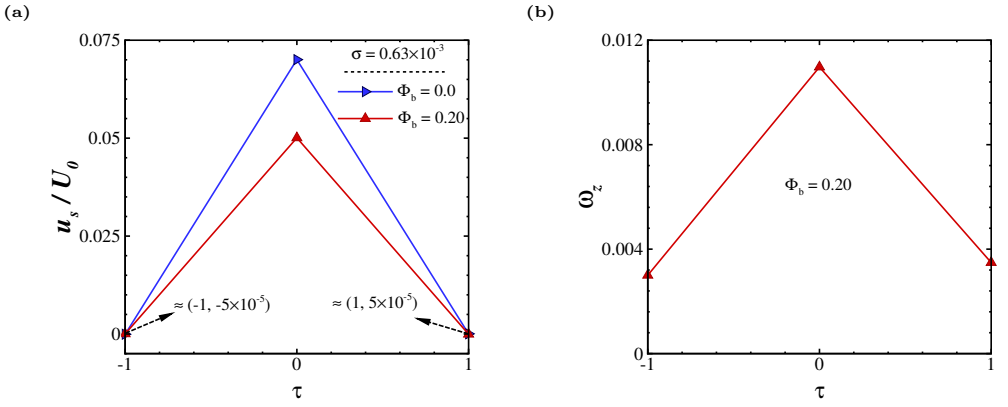

Figure 19. (a) Normalized interface slip velocity as a function of τ for different particle volume fractions under investigation at wall non-dimensional permeability parameter $\sigma = 0.63 \times 10^{-3}$. (b) Normalized spanwise component of the particle angular velocity as a function of τ for particle volume fractions $\Phi_b = 0.20$.

of the porous media. Note that the case $\tau = 0$, as reported in the previous sections, is used as the reference case.

Figure 17(a) shows the friction Reynolds number Re_τ, where we observe a significant drag increase for a nonzero momentum transfer coefficient τ. Note that Re_τ is calculated using the mean pressure gradient needed to keep U_0 constant. Decreasing the slip velocity and particle rotation causes a decrease in the particle concentration near the interface as shown in figure 17(b), where we note that the particle wall layer is significantly less pronounced when there is a net stress transferred from the porous matrix to the free fluid ($\tau \neq 0$). The data in the figure also show that for nonzero values of τ, the local maximum of the particle distribution near the channel centerline increases considerably.

Figure 18 shows the mean velocity profiles for the three momentum transfer coefficients considered. Figure 18(a) shows the velocity profile pertaining to the single-phase flow over porous media, $\Phi_b = 0$, whereas Figure 18(b) reports the data for $\Phi_b = 0.20$. The dashed line represents the case with the positive τ, the dash-dot-dotted line shows the case with the negative τ, and the solid line shows our reference case where the momentum transfer coefficient $\tau = 0$. The effect of the momentum transfer coefficient τ on the mean velocity profile are clear, especially at the suspension-porous interface: a nonzero value of τ induces a significant decrease in the velocity at the suspension-porous interface for both cases of highly-dense ($\Phi_b = 0.20$) and single phase case ($\Phi_b = 0$), while a different behaviour is observed at the centerline for the two cases. For the pure fluid $\Phi_b = 0$, the non-zero τ induces an increase in the velocity at the centerline. However, for the highly-dense case, a velocity decrease can be observed at the centerline for the nonzero values of the momentum transfer coefficient. The results for the pure fluid flow over the porous layer are in agreement with previous works (Tilton & Cortelezzi 2008; Rosti *et al.* 2015).

The normalized slip velocities for different cases studied here are shown in figure 19(a). This figure shows that the slip velocities for nonzero momentum transfer coefficient τ are much smaller than for the case $\tau = 0$ in both single-phase flow ($\Phi_b = 0$) and $\Phi_b = 0.20$. Note also that, even for larger permeabilities, previous works observed the same trend for the slip velocity for both positive and negative τ; see, for example, the results for a single-phase flow over porous media in Rosti *et al.* (2015). Figure 19(b) displays the normalized spanwise component of the mean particle angular velocity for the different momentum

transfer coefficients τ under consideration. Note that the values have been averaged over all particles close to the interface. These data reveal that the particle average angular velocity decreases significantly for values of the momentum transfer coefficient τ different from zero, consistent with the trend exhibited by the slip velocity.

The variations in the root-mean-square (r.m.s.) of the fluid velocity fluctuations with the momentum transfer coefficient τ are depicted in figure 20 for the flows at particle volume fraction $\Phi_b = 0.20$. The magnitude of the root-mean-square (r.m.s.) of the streamwise fluid velocity fluctuations decreases for nonzero τ. The same can be seen for the wall-normal and spanwise velocity fluctuations, although the reduction appears to be less pronounced and more evident outside the viscous wall layer. The results therefore confirm the reduction in turbulent transport observed from the momentum budget shown in figure 21.

To better understand the modifications on the dynamics and on the overall drag induced by a different stress condition at the wall, we also performed the momentum budget analysis; see eq. (3.1) and relative discussion. The results of this analysis are displayed in Figure 21. For the pure fluid $\Phi_b = 0$, by changing the momentum transfer coefficient from zero to -1 and 1, τ^{visc} increases and τ^{reyn} decreases. As a result, despite the attenuation of the turbulence, the overall drag increases due to the increase in the viscous stresses. For the case of a dense suspension, $\Phi_b = 0.20$, we see that the attenuation of the turbulence is relatively more important, which can be explained by the increased particle migration toward the channel core region (see figure 17(b)). However, the formation of a relatively densed packed region causes an increase in the particle stresses which more than balances the decrease in turbulent transport. As a consequence, the drag increase at $\Phi_b = 0.20$ is more pronounced for $\tau = \pm 1$. These results indicate that the condition at the suspension-porous interface has a significant impact on the flow and particle dynamics for the permeability of the porous medium considered here.

4. Conclusion

We employed direct numerical simulations to study turbulent suspension flows in a channel covered with isotropic porous media on the top and bottom surfaces. The VANS equations are used to describe the volume-averaged flow inside the porous layer, with the permeable wall characterized by permeability and porosity. We then coupled VANS with the IBM to resolve particle-particle and particle-fluid interactions. Here, we have kept the Reynolds number $Re = \frac{U_0 h}{\nu} = 5600$ and investigated the effect of particle volume fractions Φ_b, non-dimensional permeability parameter σ, and the momentum transfer coefficient τ of the porous layer for spherical and neutrally buoyant rigid particles.

Using the Reynolds turbulent friction number, Re_τ, i.e., the response to determining the turbulent drag based on the friction velocity, we quantitatively show that turbulent stress increases with both particle volume fraction Φ_b and wall non-dimensional permeability parameter σ. Overall, we observed that wall permeability is associated with higher drag due to increased turbulence activity compared to pure solvent. Turbulent suspension flows over hyperelastic materials have also been reported in (Rosti & Brandt 2017). Although some experiments for pure fluid flowing over porous surfaces show that wall permeability causes an increase in skin friction in the turbulent-flow regime (Zagni & Smith 1976; Zippe & Graf 1983), others reveal a decrease in the skin friction in the laminar-flow regime such as (Beavers & Joseph 1967).

Because the channel top and bottom walls have an isotropic porous medium, the velocity profile in the free-flow region remains the same as if the walls were smooth, as

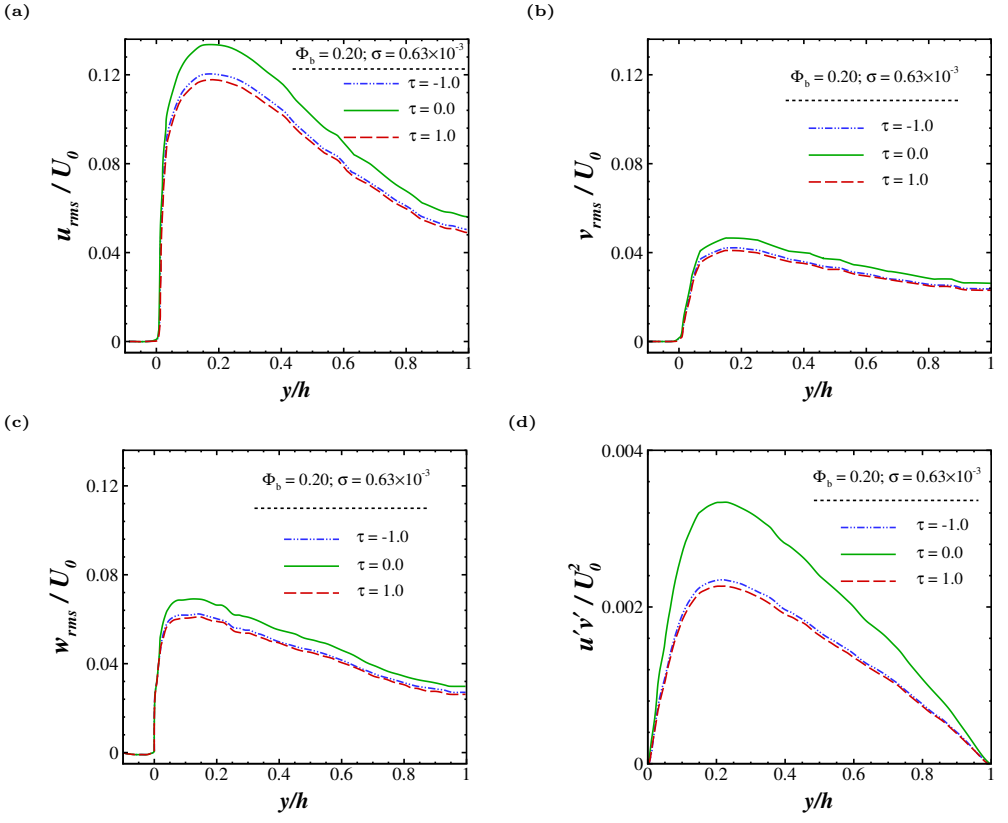

Figure 20. Intensity of the fluid fluctuation velocity components normalized by U_0 and the Reynolds shear stress for different τ and a fixed particle volume fraction $\Phi_b = 0.20$ and non-dimensional permeability parameter $\sigma = 0.63 \times 10^{-3}$: (a) streamwise u_{rms}; (b) wall-normal v_{rms}; (c) spanwise w_{rms} velocity fluctuations; and (d) shear stress $(uv)'$.

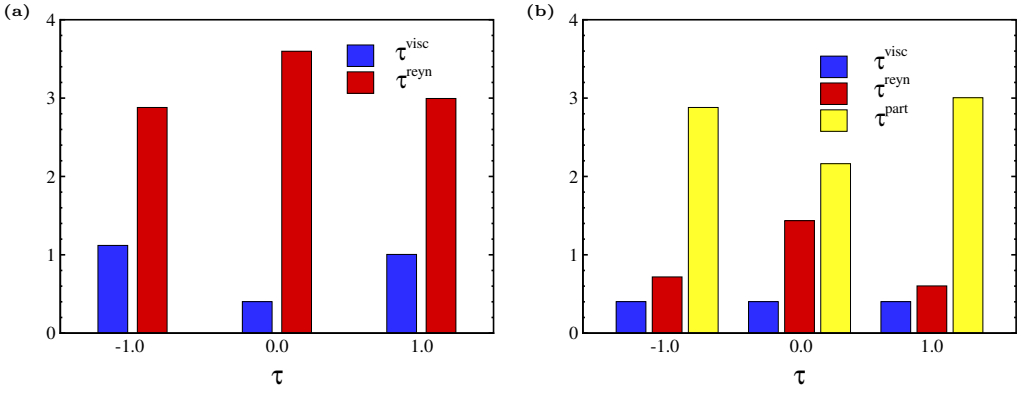

Figure 21. Histograms showing the different components of the mean shear stress balance as a function of τ for (a) $\Phi_b = 0.0$ and (b) $\Phi_b = 0.20$. Blue, red and yellow show the viscous stress, Reynolds shear stress and particle contributions, respectively.

reported in (Picano *et al.* 2015), but a slip velocity u_s is generated at the suspension-porous interface. In our study, we found that the slip velocity u_s decreases with increasing particle volume fraction Φ_b. By contrast, when the permeability of the wall increases, the slip velocity increases. In general, the decrease in particle-particle interaction results from increasing the slip velocity u_s with the wall permeability parameter σ.

Our analysis of the flow streamwise momentum balance showed that as particle volume fraction increases, the additional stress due to particles increases. For instance, at $\Phi_\mathrm{b} = 0.20$, the particle stress dominates the flow, while Reynolds transport dominates at $\Phi_\mathrm{b} = 0$ and $\Phi_\mathrm{b} < 0.2$. It is also shown that adding more particles increases particle-induced stresses, which causes drag to increase. While turbulent stresses decay rapidly with increasing particle volume fractions, viscous stresses remain nearly constant.

A final analysis was performed on the statistics of turbulence caused by momentum transfer coefficients τ. Slip velocity decreases noticeably when momentum transfer coefficient τ is changed. Based on our studies, we found that for a nonzero momentum transfer coefficient, the average particle angular velocity near the wall is lower than $\tau = 0$. The other noticeable effect of the momentum transfer coefficient τ on the concentration profile, where nonzero τ leads to the migration of particles to the center of the channel, which means that fewer particles gather near the free flow and porous interface compared to $\tau = 0$. Increasing particle contribution also decreases Reynolds shear stress, thereby reducing total shear stress. The results also show that τ has a considerable effect on the behavior of turbulent suspension flow over porous media; therefore, we need to consider the momentum transfer coefficient as an essential factor in future studies.

To further improve this study, other important factors can be considered. We should certainly pay attention to the effect of particle size (Lashgari *et al.* 2017), shape (Bellani *et al.* 2012) and deformability (Alghalibi *et al.* 2019) as new insights to our current study. In addition, experiments are needed to verify our results. We assumed that particles in this study would not be able to enter the porous layer due to their size. Understanding whether the same behavior occurs when particles move inside the porous media and the impact of anisotropic porous media will be the subject of our future investigation.

Acknowledgements. PM was supported by the National Science Foundation (Award No. 1854376) and by the Army Research Office (Award No. W911NF-18-1-0356). The work of SMA and AMB was funded by National Science Foundation (Award No. 1854376). LB acknowledges financial support from the Swedish Research Council (VR) through the INTERFACE research environment (Grant No. VR 2016-06119).

Declaration of interests. The authors report no conflict of interest.

REFERENCES

Alazmi, B & Vafai, K 2001 Analysis of fluid flow and heat transfer interfacial conditions between a porous medium and a fluid layer. *International Journal of Heat and Mass Transfer* **44** (9), 1735–1749.

Alghalibi, Dhiya, Rosti, Marco E & Brandt, Luca 2019 Inertial migration of a deformable particle in pipe flow. *Physical Review Fluids* **4** (10), 104201.

Ardekani, MN, Rosti, Marco Edoardo & Brandt, Luca 2019 Turbulent flow of finite-size spherical particles in channels with viscous hyper-elastic walls. *J. Fluid Mech.* **873**, 410–440.

Ardekani, Mehdi Niazi, Al Asmar, Léa, Picano, Francesco & Brandt, Luca 2018 Numerical study of heat transfer in laminar and turbulent pipe flow with finite-size spherical particles. *Int. J. Heat Fluid Flow* **71**, 189–199.

Ardekani, M Niazi & Brandt, Luca 2019 Turbulence modulation in channel flow of finite-size spheroidal particles. *Journal of Fluid Mechanics* **859**, 887–901.

Ardekani, Mehdi Niazi, Costa, Pedro, Breugem, Wim Paul & Brandt, Luca 2016 Numerical study of the sedimentation of spheroidal particles. *International Journal of Multiphase Flow* **87**, 16–34.

Ardekani, M Niazi, Costa, Pedro, Breugem, W-P, Picano, Francesco & Brandt, Luca 2017 Drag reduction in turbulent channel flow laden with finite-size oblate spheroids. *Journal of Fluid Mechanics* **816**, 43–70.

Bagheri, Maryam, Kang, Changwoo & Mirbod, Parisa 2019 Suspension flows in a pipe covered with permeable surfaces. In *APS Division of Fluid Dynamics Meeting Abstracts*, pp. NP05–020.

Bagheri, Maryam & Mirbod, Parisa 2022 Effect of porous media models on rheological properties of suspensions. *Journal of Non-Newtonian Fluid Mechanics* **307**, 104876.

Bagheri, Maryam, Moradi Bilondi, Abbas, Taheri, Elmira, Anand, Aayush, Schatz, Michael F & Mirbod, Parisa 2022 An experimental analysis of flow transitions in a periodically grooved channel. In *APS Division of Fluid Dynamics Meeting Abstracts*.

Bear, Jacob 1988 *Dynamics of fluids in porous media*. Courier Corporation.

Beavers, Gordon S & Joseph, Daniel D 1967 Boundary conditions at a naturally permeable wall. *Journal of fluid mechanics* **30** (1), 197–207.

Bec, Jeremie, Biferale, Luca, Cencini, Massimo, Lanotte, Alessandra, Musacchio, Stefano & Toschi, Federico 2007 Heavy particle concentration in turbulence at dissipative and inertial scales. *Physical review letters* **98** (8), 084502.

Bellani, Gabriele, Byron, Margaret L, Collignon, Audric G, Meyer, Colin R & Variano, Evan A 2012 Shape effects on turbulent modulation by large nearly neutrally buoyant particles. *Journal of Fluid Mechanics* **712**, 41–60.

Biegert, Edward, Vowinckel, Bernhard & Meiburg, Eckart 2017 A collision model for grain-resolving simulations of flows over dense, mobile, polydisperse granular sediment beds. *Journal of Computational Physics* **340**, 105–127.

Brenner, Howard 1961 The slow motion of a sphere through a viscous fluid towards a plane surface. *Chemical engineering science* **16** (3-4), 242–251.

Breugem, WP, Boersma, BJ & Uittenbogaard, RE 2004 Direct numerical simulations of plane channel flow over a 3d cartesian grid of cubes. In *Proc. Intl Conf. on Applications of Porous Media (ed. AH Reis & AF Miguel)*, pp. 27–34.

Breugem, WP, Boersma, BJ & Uittenbogaard, RE 2006 The influence of wall permeability on turbulent channel flow. *Journal of Fluid Mechanics* **562**, 35.

Breugem, Wim-Paul 2012 A second-order accurate immersed boundary method for fully resolved simulations of particle-laden flows. *Journal of Computational Physics* **231** (13), 4469–4498.

Breugem, Wim-Paul & Boersma, Bendiks-Jan 2005 Direct numerical simulations of turbulent flow over a permeable wall using a direct and a continuum approach. *Physics of fluids* **17** (2), 025103.

Brinkman, HC 1947 Fluid flow in a porous medium. *Appl. Sci. Res. A* **27** (143149), 42.

Carotenuto, Claudia & Minale, Mario 2011 Shear flow over a porous layer: Velocity in the real proximity of the interface via rheological tests. *Physics of Fluids* **23** (6), 063101.

Chandesris, M & Jamet, D 2006 Boundary conditions at a planar fluid–porous interface for a poiseuille flow. *International Journal of Heat and Mass Transfer* **49** (13-14), 2137–2150.

Chandesris, M & Jamet, D 2007 Boundary conditions at a fluid–porous interface: an a priori estimation of the stress jump coefficients. *International journal of heat and mass transfer* **50** (17-18), 3422–3436.

Chen, Hao, Wang, Jiabing & Yang, Kun 2016 Analysis of the momentum transport boundary conditions at a fluid-porous interface. In *Heat Transfer Summer Conference*, , vol. 50329, p. V001T03A006. American Society of Mechanical Engineers.

Costa, Pedro, Boersma, Bendiks Jan, Westerweel, Jerry & Breugem, Wim-Paul 2015 Collision model for fully resolved simulations of flows laden with finite-size particles. *Physical Review E* **92** (5), 053012.

Costa, Pedro, Picano, Francesco, Brandt, Luca & Breugem, Wim-Paul 2016 Universal

scaling laws for dense particle suspensions in turbulent wall-bounded flows. *Phys. Rev. Lett.* **117** (13), 134501.

Costa, Pedro, Picano, Francesco, Brandt, Luca & Breugem, Wim-Paul 2018 Effects of the finite particle size in turbulent wall-bounded flows of dense suspensions. *J. Fluid Mech.* **843**, 450–478.

Darcy, Henry Philibert Gaspard 1856 *Les Fontaines publiques de la ville de Dijon. Exposition et application des principes à suivre et des formules à employer dans les questions de distribution d'eau, etc*. V. Dalamont.

Deng, C & Martinez, DM 2005 Viscous flow in a channel partially filled with a porous medium and with wall suction. *Chemical Engineering Science* **60** (2), 329–336.

Francesco Lucci, Antonio Ferrante & Elghobashi, Said 2010 Modulation of isotropic turbulence by particles of taylor length-scale size. *J. Fluid Mech.* **650**, 5–55.

Giorgi, Tiziana 1997 Derivation of the forchheimer law via matched asymptotic expansions. *Transport in porous media* **29** (2), 191–206.

Goyeau, B, Lhuillier, D, Gobin, D & Velarde, MG 2003*a* Momentum transport at a fluid–porous interface. *International Journal of Heat and Mass Transfer* **46** (21), 4071–4081.

Goyeau, B, Lhuillier, D, Gobin, D & Velarde, MG 2003*b* Momentum transport at a fluid–porous interface. *International Journal of Heat and Mass Transfer* **46** (21), 4071–4081.

Haffner, Eileen, Kang, Changwoo, Shapley, Nina & Mirbod, Parisa 2019 Experimental and numerical studies of particle-laden fluid flows over a porous media model. In *APS Division of Fluid Dynamics Meeting Abstracts*, pp. B04–005.

Haffner, Eileen A & Mirbod, Parisa 2020 Velocity measurements of dilute particulate suspension over and through a porous medium model. *Physics of Fluids* **32** (8), 083608.

Hahn, Seonghyeon, Je, Jongdoo & Choi, Haecheon 2002 Direct numerical simulation of turbulent channel flow with permeable walls. *Journal of Fluid Mechanics* **450**, 259.

Herwig, Andreas, Kempe, Tobias & Fröhlich, Jochen 2011 Phase resolved dns of the turbulent flow over a sediment bed and analysis of the erosion process. *PAMM* **11** (1), 611–612.

Hooshyar, Saman, Yoshikawa, Harunori N & Mirbod, Parisa 2022 The impact of imposed couette flow on the stability of pressure-driven flows over porous surfaces. *Journal of Engineering Mathematics* **132** (1), 1–22.

Itoh, Motoyuki, Tamano, Shinji, Iguchi, Ryo, Yokota, Kazuhiko, Akino, Norio, Hino, Ryutaro & Kubo, Shinji 2006 Turbulent drag reduction by the seal fur surface. *Physics of Fluids* **18** (6), 065102.

Izbassarov, Daulet, Rosti, Marco E, Ardekani, M Niazi, Sarabian, Mohammad, Hormozi, Sarah, Brandt, Luca & Tammisola, Outi 2018 Computational modeling of multiphase viscoelastic and elastoviscoplastic flows. *International Journal for Numerical Methods in Fluids* **88** (12), 521–543.

Jain, Ramandeep, Tschisgale, Silvio & Froehlich, Jochen 2020 Effect of particle shape on bedload sediment transport in case of small particle loading. *Meccanica* **55** (2), 299–315.

Jain, Ramandeep, Tschisgale, Silvio & Fröhlich, Jochen 2021 Impact of shape: Dns of sediment transport with non-spherical particles. *Journal of Fluid Mechanics* **916**.

Jimenez, Javier, Uhlmann, Markus, Pinelli, Alfredo & Kawahara, Genta 2001 Turbulent shear flow over active and passive porous surfaces. *Journal of Fluid Mechanics* **442**, 89–117.

Joseph, Daniel D, Nield, Donald A & Papanicolaou, George 1982 Nonlinear equation governing flow in a saturated porous medium. *Water Resources Research* **18** (4), 1049–1052.

Kang, Changwoo & Mirbod, Parisa 2019 Porosity effects in laminar fluid flow near permeable surfaces. *Physical Review E* **100** (1), 013109.

Kang, Changwoo & Mirbod, Parisa 2021 Pressure-driven pipe flow of semi-dilute and dense suspensions over permeable surfaces. *Rheologica Acta* **60** (11), 711–718.

Kempe, Tobias, Vowinckel, Bernhard & Fröhlich, Jochen 2014 On the relevance of collision modeling for interface-resolving simulations of sediment transport in open channel flow. *International journal of multiphase flow* **58**, 214–235.

Kidanemariam, Aman G, Chan-Braun, Clemens, Doychev, Todor & Uhlmann, Markus

2013 Direct numerical simulation of horizontal open channel flow with finite-size, heavy particles at low solid volume fraction. *New Journal of Physics* **15** (2), 025031.

Kidanemariam, Aman G & Uhlmann, Markus 2014 Direct numerical simulation of pattern formation in subaqueous sediment. *Journal of Fluid Mechanics* **750**.

Köllner, Thomas, Meredith, Alex, Nokes, Roger & Meiburg, Eckart 2020 Gravity currents over fixed beds of monodisperse spheres. *Journal of Fluid Mechanics* **901**.

Kong, F & Schetz, J 1982 Turbulent boundary layer over porous surfaces with different surfacegeometries. In *20th Aerospace Sciences Meeting*, p. 30.

Kuwata, Y & Suga, K 2016 Lattice boltzmann direct numerical simulation of interface turbulence over porous and rough walls. *International Journal of Heat and Fluid Flow* **61**, 145–157.

Kuwata, Y & Suga, K 2017 Direct numerical simulation of turbulence over anisotropic porous media. *Journal of Fluid Mechanics* **831**, 41–71.

Lage, J 1998 The fundamental theory of flow through permeable niedia from darcy to turbulence. *Transport phenomena in porous media* **1**.

Lashgari, Iman, Picano, Francesco, Breugem, Wim-Paul & Brandt, Luca 2014 Laminar, turbulent, and inertial shear-thickening regimes in channel flow of neutrally buoyant particle suspensions. *Phys. Rev. Lett.* **113** (25), 254502.

Lashgari, Iman, Picano, Francesco, Costa, Pedro, Breugem, Wim-Paul & Brandt, Luca 2017 Turbulent channel flow of a dense binary mixture of rigid particles. *Journal of Fluid Mechanics* **818**, 623–645.

Loisel, Vincent, Abbas, Micheline, Masbernat, Olivier & Climent, Eric 2013 The effect of neutrally buoyant finite-size particles on channel flows in the laminar-turbulent transition regime. *Physics of Fluids* **25** (12), 123304.

Matas, Jean-Philippe, Morris, Jeffrey F & Guazzelli, Élisabeth 2004 Inertial migration of rigid spherical particles in poiseuille flow. *Journal of Fluid Mechanics* **515**, 171–195.

Min, Jung Yim & Kim, Sung Jin 2005 A novel methodology for thermal analysis of a composite system consisting of a porous medium and an adjacent fluid layer. *J. Heat Transfer* **127** (6), 648–656.

Minale, Mario 2014*a* Momentum transfer within a porous medium. i. theoretical derivation of the momentum balance on the solid skeleton. *Physics of Fluids* **26**, 123101.

Minale, Mario 2014*b* Momentum transfer within a porous medium. ii. stress boundary condition. *Physics of Fluids* **26**, 123102.

Mirbod, P, Andreopoulos, Y & Weinbaum, S 2009 On the generation of lift forces in random soft porous media. *Journal of fluid mechanics* **619**, 147–166.

Mirbod, Parisa & Shapley, Nina C 2022 Particle migration of suspensions in a pressure-driven flow over and through a porous structure. *Journal of Rheology* .

Mirbod, Parisa, Wu, Zhenxing & Ahmadi, Goodarz 2017 Laminar flow drag reduction on soft porous media. *Scientific reports* **7** (1), 1–10.

Mittal, Rajat & Iaccarino, Gianluca 2005 Immersed boundary methods. *Annu. Rev. Fluid Mech.* **37**, 239–261.

Moradi Bilondi, Abbas, Mastroianni, Nazario, Brandt, Luca & Mirbod, Parisa 2022 Turbulent flow of polymer solutions in a square duct roughened with transverse ribs. In *APS Division of Fluid Dynamics Meeting Abstracts*.

Neale, Graham & Nader, Walter 1974 Practical significance of brinkman's extension of darcy's law: coupled parallel flows within a channel and a bounding porous medium. *The Canadian Journal of Chemical Engineering* **52** (4), 475–478.

Ochoa-Tapia, J Alberto & Whitaker, Stephen 1995 Momentum transfer at the boundary between a porous medium and a homogeneous fluid—i. theoretical development. *International Journal of Heat and Mass Transfer* **38** (14), 2635–2646.

Pan, Y & Banerjee, S 1996 Numerical simulation of particle interactions with wall turbulence. *Physics of Fluids* **8** (10), 2733–2755.

Papadopoulos, Konstantinos, Nikora, Vladimir, Vowinckel, Bernhard, Cameron, Stuart, Jain, Ramandeep, Stewart, Mark, Gibbins, Christopher & Fröhlich, Jochen 2020 Double-averaged kinetic energy budgets in flows over mobile granular beds: insights from dns data analysis. *Journal of Hydraulic Research* **58** (4), 653–672.

Peng, Cheng, Ayala, Orlando M & Wang, Lian-Ping 2019 A direct numerical investigation of two-way interactions in a particle-laden turbulent channel flow. *J. Fluid Mech.* **875**.

Peng, Cheng & Wang, Lian-Ping 2020 Force-amplified, single-sided diffused-interface immersed boundary kernel for correct local velocity gradient computation and accurate no-slip boundary enforcement. *Physical Review E* **101** (5), 053305.

Perot, Blair & Moin, Parviz 1995 Shear-free turbulent boundary layers. part 1. physical insights into near-wall turbulence. *Journal of Fluid Mechanics* **295**, 199–228.

Peskin, Charles S 1972 Flow patterns around heart valves: a numerical method. *Journal of computational physics* **10** (2), 252–271.

Picano, Francesco, Breugem, Wim-Paul & Brandt, Luca 2015 Turbulent channel flow of dense suspensions of neutrally buoyant spheres. *Journal of Fluid Mechanics* **764**, 463–487.

Quintard, Michel & Whitaker, Stephen 1994 Transport in ordered and disordered porous media ii: Generalized volume averaging. *Transport in porous media* **14** (2), 179–206.

Reeks, MW 1983 The transport of discrete particles in inhomogeneous turbulence. *Journal of aerosol science* **14** (6), 729–739.

Rosti, Marco E & Brandt, Luca 2017 Numerical simulation of turbulent channel flow over a viscous hyper-elastic wall. *Journal of Fluid Mechanics* **830**, 708–735.

Rosti, Marco Edoardo & Brandt, Luca 2020 Increase of turbulent drag by polymers in particle suspensions. *Physical Review Fluids* **5** (4), 041301.

Rosti, Marco Edoardo, Brandt, Luca & Pinelli, Alfredo 2018 Turbulent channel flow over an anisotropic porous wall-drag increase and reduction. *Journal of Fluid Mechanics* **842**, 381–394.

Rosti, Marco E, Cortelezzi, Luca & Quadrio, Maurizio 2015 Direct numerical simulation of turbulent channel flow over porous walls. *Journal of Fluid Mechanics* **784**, 396–442.

Rosti, Marco E, Mirbod, Parisa & Brandt, Luca 2021 The impact of porous walls on the rheology of suspensions. *Chemical Engineering Science* p. 116178.

Rosti, Marco Edoardo, Pramanik, Satyajit, Brandt, Luca & Mitra, Dhrubaditya 2020 The breakdown of darcy's law in a soft porous material. *Soft matter* **16** (4), 939–944.

Ruff, JF & Gelhar, LW 1972 Turbulent shear flow in porous boundary. *J. Engrg. Mech* **504** (98), 975.

Sardina, G, Schlatter, Philipp, Brandt, Luca, Picano, F & Casciola, Carlo Massimo 2012 Wall accumulation and spatial localization in particle-laden wall flows. *Journal of Fluid Mechanics* **699** (1), 50–78.

Gomez-de Segura, G, Sharma, A & García-Mayoral, R 2017 Turbulent drag reduction by anisotropic permeable coatings. In *10th International Symposium on Turbulence and Shear Flow Phenomena-TSFP10*.

Shao, Xueming, Wu, Tenghu & Yu, Zhaosheng 2012 Fully resolved numerical simulation of particle-laden turbulent flow in a horizontal channel at a low reynolds number. *Journal of Fluid Mechanics* **693**, 319.

Song, Wang, Jinzhou, Zhao & Yongming, Li 2014 Hydraulic fracturing simulation of complex fractures growth in naturally fractured shale gas reservoir. *Arabian Journal for Science and Engineering* **39** (10), 7411–7419.

Suga, K, Matsumura, Y, Ashitaka, Y, Tominaga, S & Kaneda, M 2010 Effects of wall permeability on turbulence. *International Journal of Heat and Fluid Flow* **31** (6), 974–984.

Suga, Kazuhiko, Nakagawa, Yuka & Kaneda, Masayuki 2017 Spanwise turbulence structure over permeable walls. *Journal of Fluid Mechanics* **822**, 186.

Tilton, Nils & Cortelezzi, Luca 2008 Linear stability analysis of pressure-driven flows in channels with porous walls. *Journal of Fluid Mechanics* **604**, 411.

Toschi, Federico & Bodenschatz, Eberhard 2009 Lagrangian properties of particles in turbulence. *Annual review of fluid mechanics* **41**, 375–404.

Uhlmann, Markus 2005 An immersed boundary method with direct forcing for the simulation of particulate flows. *Journal of Computational Physics* **209** (2), 448–476.

Vafai, K & Kim, SungJin 1990 Fluid mechanics of the interface region between a porous medium and a fluid layer—an exact solution. *International Journal of Heat and Fluid Flow* **11** (3), 254–256.

Vafai, Kambiz & Thiyagaraja, Rajaraman 1987 Analysis of flow and heat transfer at the

interface region of a porous medium. *International Journal of Heat and Mass Transfer* **30** (7), 1391–1405.

Valdés-Parada, Francisco J, Aguilar-Madera, Carlos G, Ochoa-Tapia, J Alberto & Goyeau, Benoît 2013 Velocity and stress jump conditions between a porous medium and a fluid. *Advances in water resources* **62**, 327–339.

Valdés-Parada, Francisco J, Alvarez-Ramírez, José, Goyeau, Benoît & Ochoa-Tapia, J Alberto 2009 Computation of jump coefficients for momentum transfer between a porous medium and a fluid using a closed generalized transfer equation. *Transport in porous media* **78** (3), 439–457.

Valdés-Parada, Francisco J, Goyeau, Benoiˆt & Ochoa-Tapia, J Alberto 2007 Jump momentum boundary condition at a fluid–porous dividing surface: derivation of the closure problem. *Chemical engineering science* **62** (15), 4025–4039.

Vowinckel, Bernhard, Biegert, Edward, Luzzatto-Fegiz, Paolo & Meiburg, Eckart 2019*a* Consolidation of freshly deposited cohesive and noncohesive sediment: Particle-resolved simulations. *Physical Review Fluids* **4** (7), 074305.

Vowinckel, Bernhard, Biegert, Edward, Meiburg, Eckart, Aussillous, Pascale & Guazzelli, Élisabeth 2021 Rheology of mobile sediment beds sheared by viscous, pressure-driven flows. *Journal of Fluid Mechanics* **921**.

Vowinckel, Bernhard, Kempe, Tobias & Fröhlich, Jochen 2014 Fluid–particle interaction in turbulent open channel flow with fully-resolved mobile beds. *Advances in Water Resources* **72**, 32–44.

Vowinckel, Bernhard, Nikora, Vladimir, Kempe, Tobias & Fröhlich, Jochen 2017 Momentum balance in flows over mobile granular beds: application of double-averaging methodology to dns data. *Journal of Hydraulic Research* **55** (2), 190–207.

Vowinckel, B, Withers, J, Luzzatto-Fegiz, Paolo & Meiburg, E 2019*b* Settling of cohesive sediment: particle-resolved simulations. *Journal of Fluid Mechanics* **858**, 5–44.

Whitaker, Stephen 1969 Advances in theory of fluid motion in porous media. *Industrial & engineering chemistry* **61** (12), 14–28.

Whitaker, Stephen 1986 Flow in porous media i: A theoretical derivation of darcy's law. *Transport in porous media* **1** (1), 3–25.

Whitaker, Stephen 1996*a* The forchheimer equation: a theoretical development. *Transport in Porous media* **25** (1), 27–61.

Whitaker, Stephen 1996*b* The forchheimer equation: a theoretical development. *Transport in Porous media* **25** (1), 27–61.

Wu, Zhenxing & Mirbod, Parisa 2018 Experimental analysis of the flow near the boundary of random porous media. *Physics of Fluids* **30** (4), 047103.

Wu, Zhenxing & Mirbod, Parisa 2019 Instability analysis of the flow between two parallel plates where the bottom one coated with porous media. *Advances in Water Resources* **130**, 221–228.

Yeo, Kyongmin, Dong, Suchuan, Climent, Eric & Maxey, Martin R 2010 Modulation of homogeneous turbulence seeded with finite size bubbles or particles. *International Journal of Multiphase Flow* **36** (3), 221–233.

Yeo, Kyongmin & Maxey, Martin R 2010 Dynamics of concentrated suspensions of non-colloidal particles in couette flow. *Journal of Fluid Mechanics* **649**, 205.

Yousefi, Ali, Ardekani, Mehdi Niazi, Picano, Francesco & Brandt, Luca 2021 Regimes of heat transfer in finite-size particle suspensions. *International Journal of Heat and Mass Transfer* **177**, 121514.

Yu, Zhaosheng, Wu, Tenghu, Shao, Xueming & Lin, Jianzhong 2013 Numerical studies of the effects of large neutrally buoyant particles on the flow instability and transition to turbulence in pipe flow. *Physics of Fluids* **25** (4), 043305.

Zade, Sagar, Costa, Pedro, Fornari, Walter, Lundell, Fredrik & Brandt, Luca 2018 Experimental investigation of turbulent suspensions of spherical particles in a square duct. *Journal of Fluid Mechanics* **857**, 748–783.

Zagni, Anthony FE & Smith, Kenneth VH 1976 Channel flow over permeable beds of graded spheres. *Journal of the hydraulics division* **102** (2), 207–222.

Zhai, Zongyu, Sharma, Mukul Mani & others 2005 A new approach to modeling hydraulic

fractures in unconsolidated sands. In *SPE Annual Technical Conference and Exhibition*. Society of Petroleum Engineers.

Zippe, Hans J & Graf, Walter H 1983 Turbulent boundary-layer flow over permeable and non-permeable rough surfaces. *Journal of Hydraulic research* **21** (1), 51–65.